

RESEARCH TRIANGLE INSTITUTE

NASA Contractor Report No. 66476

EXPERIMENTAL VERIFICATION OF GAMMA RAY ATMOSPHERIC  
DENSITY SENSOR MATHEMATICAL MODEL PREDICTIONS

6 R. P. Gardner and D. R. Whitaker 3

(Distribution of this report is provided in the interest of information exchange. Responsibility for the contents resides in the authors or the organization that prepared it.)

Prepared for  
Langley Research Center  
National Aeronautics and Space Administration

27A  
(Prepared under Contract No. NAS1-7046, RTI Project No. NU-321, by the Measurement and Controls Laboratory of the Research Triangle Institute, Research Triangle Park, North Carolina.) 2

9 August 1967 10

FACILITY FORM 602	N67-40152	(ACCESSION NUMBER)	(THRU)
	10 7/15 25	(PAGES)	(CODE)
	Co# 66476 29B	(NASA CR OR TMX OR AD NUMBER)	(CATEGORY)

RESEARCH TRIANGLE PARK, NORTH CAROLINA 27709

## ABSTRACT

The gamma-ray scattering technique shows promise for use in the continuous measurement of atmospheric density from space vehicles. Mathematical models have been derived to predict the performance, identify problem areas, and explain the data taken on two flight tests of prototype devices. Design parameters such as gamma-ray source energy, source-to-detector separation, detector discriminator settings, and shield effectiveness were studied in an attempt to understand and optimize this technique. Subsequently, experimental studies were made to verify and improve (determine constants for) these mathematical models. The experimental results agreed quite well with the model predictions and prove the effectiveness of this method for optimizing the design of the gamma-ray atmospheric density sensor.

## Table of Contents

	Page
Abstract . . . . .	ii
1. Summary . . . . .	1
2. Introduction . . . . .	2
3. Experimental Verification of Model Predictions Regarding Unshielded Source . . . . .	4
3.1 Experimental Apparatus . . . . .	5
3.2 Model Predictions . . . . .	8
3.3 Calibration of Sources . . . . .	9
3.4 Experimental Results . . . . .	13
3.5 Comparison of Experimental Results with Predicted Values . . .	14
3.6 Conclusions . . . . .	17
4. Experimental Verification of Model Predictions Regarding Shielded Source . . . . .	18
4.1 Experimental Apparatus . . . . .	19
4.2 Experimental Results . . . . .	20
4.3 Model Predictions . . . . .	22
4.4 Comparison of Experimental Results with Predicted Values . . .	24
4.5 Conclusions . . . . .	30
5. Recommendation for Continuation of Phase II . . . . .	31
References . . . . .	32
Figures . . . . .	33
Tables . . . . .	49

## 1. Summary

This report documents the results of an experimental program undertaken to verify (and determine constants for) the mathematical models that were used to predict the performance, identify problem areas, and explain the data taken on two flight tests of a gamma-ray scatter gauge for measuring atmospheric density. In this experimental program we measured the response of a prototype gauge to both density and the multiple scattering of gamma rays down the vehicle walls. The tests were performed in a 60 foot diameter vacuum sphere at the NASA-Langley Research Center. Three parameters which were varied during the tests were gamma-ray energy, wall thickness, and source-to-detector distance.

Examination of the experimental and model predictions indicated that the predictions for the gauge response to density were quite good. At the larger source-to-detector distance the ratios of experimental to predicted were 0.918, 0.996, and 1.001 for  $^{241}\text{Am}$ ,  $^{153}\text{Gd}$ , and  $^{57}\text{Co}$ , respectively, and 0.645, 0.726, and 0.734 for the closer source-to-detector distance. The wall streaming experimental results, as expected, were much higher than the values predicted by our model which we know represents a minimum prediction. It is concluded that multiple scattering of the primary, low-energy gamma rays down the rocket walls does account for the major part of the previously unexplained high background response observed in the two flight tests.

Results of the experiments designed to explain the surprising data found on the second flight test in which the source was alternately exposed and shielded with a tungsten cup indicate that the tungsten shield did not contribute significantly to the generation of bremsstrahlung as was previously thought. A very low number of 0.134 Mev gamma rays were emitted from the source because of source self-absorption. The ratios of predicted shield open to shield closed responses for **density** and wall streaming (background) were 1.74 and 1-30, respectively, as compared to the values 3.00 and 0.92 found experimentally. In view of the assumptions that had to be made and the inconsistency found in the experimental results, this represents a reasonable substantiation of the model predictions.

A recommendation to develop a more comprehensive model of wall streaming in which Monte Carlo techniques would be helpful is made.

## 2. Introduction

In our previous work (Ref. 3) under Contract No. NAS1-5467 we derived theoretical, mathematical models to predict the performance, identify problem areas, and explain the data taken on two flight tests of a gamma-ray scatter gauge for measuring atmospheric density. These models predicted that the gauge response was linear with atmospheric density, independent of atmospheric composition if gamma-ray energies larger than 0.1 Mev are employed, affected by atmospheric density as far as 10 meters from the rocket, and independent of shock wave perturbations that are likely to be encountered. Significant problems identified were: (1) inaccurate calibration technique, (2) a high background response due to gamma-ray streaming down the rocket wall, and (3) a dependence on atmospheric composition if gamma-ray energies less than 0.1 Mev are used. The reader is referred to Refs. 1 and 2 for detailed discussions and results of the flight tests and to Ref. 3 for detailed discussions and results of the mathematical model studies.

In addition to the problems discussed above, one puzzling data anomaly was observed on the second flight test when a small tungsten cup was used to attenuate the  $^{144}\text{Ce} - ^{144}\text{Pr}$  source in one-second cycles. The counting rate with each detector was found to be reduced by only a factor of two for air at sea level when the source was attenuated by the tungsten cup. The counting rates at essentially zero air density were reversed; that is, the counting rates of the detectors with the attenuator cup over the source were slightly higher than when the source was exposed. We predicted that the production of bremsstrahlung by the high-energy beta particles from  $^{144}\text{Ce}$  would account for these puzzling results.

An experimental program was undertaken under the present Contract No. NAS1-7046 to verify the mathematical models described earlier and to demonstrate the hypothesis that bremsstrahlung would account for the unexpected gauge response on the second flight test. The purpose of Task 1 of this contract was to verify that the high background level observed on the prototype density sensor flight tests was due to streaming of low energy gamma rays within the skin of the vehicle when the source was unshielded. The purpose of Task 2 of the contract was to verify that the high background level observed on the prototype density sensor flight tests with the source shielded by a tungsten cup was due to streaming of bremsstrahlung gamma rays within the vehicle skin.

This report presents the results of the Phase I experimental program of Contract No. NAS1-7046. It therefore represents Task 5 of Phase I which requires a documentation

of the results of the experimental program performed under Tasks 1 and 2 described above.

The primary objectives of the present study were: (1) to verify our previous prediction that the unexplained high background response of the flight-tested gauges was due to the multiple scatter of gamma rays down the space vehicle walls and subsequently into the detector, (2) to determine factors which will allow the model-predicted minimum amount of multiple scattering down the space vehicle walls to be adjusted to correct values, and (3) to demonstrate the hypothesis that the production of bremsstrahlung by the high-energy beta particles from  $^{144}\text{Ce}$  would account for the gauge response of the second flight test which incorporated a tungsten cup as an alternating shield over the  $^{144}\text{Ce}$  source. The first two of these objectives is treated in Sec. 3 while the third objective is treated in Sec. 4.

### 3. Experimental Verification of Model Predictions Regarding Unshielded Source

In our previous work (Ref. 3) we predicted that about 53 percent of the unexplained high background response was due to the multiple scattering of the primary (low-energy) gamma rays from the source down the rocket walls and into the detector. This prediction was on the basis of a 21.4-curie source with negligible self absorption. If we assume that the amount of self absorption present was measured by the ratio of the experimental response to the model-predicted response for the density of standard air, then the corrected background response predicted would represent 27.2 percent of that observed. Our model represents a minimum prediction since only the case of one scatter in the wall adjacent to the source and one scatter in the wall adjacent to the detector was treated. Only those gamma rays moving directly down the wall were taken into account and all scattering events were assumed to remove the affected gamma rays entirely. This led us to suspect that essentially all of the unexplained high background response could be explained by multiple scattering down the vehicle wall, since it was reasonable to assume that our model-predicted minimum could easily be low by a factor of 3.7 which is equivalent to the 27.2 percent prediction.

To investigate this hypothesis experimentally, we decided to determine the response of a prototype gauge to both density and to the multiple scattering of gamma rays down the rocket walls. This procedure was desirable since our basic model which describes the response to atmospheric density would also be checked. Most of the individual parts of both programs are identical (such as scattering cross sections and detector efficiencies) and therefore a check on both models would insure that no bias would be present in the verification of the hypothesis that our model for predicting the multiple scattering of gamma rays down the rocket wall represents a minimum that must be corrected empirically or by use of a more sophisticated model. Such a program would also give generally useful information, since a primary programmatic interest is the signal-to-noise ratio and the design factors that influence this ratio.

To prove the wall-streaming hypothesis and to determine the appropriate factors to apply to our model, we undertook an experimental program to measure the amount of multiple wall scattering from low-energy, gamma-ray sources. To compare with the model predictions the experimental program included varying three parameters: gamma-ray energy, wall thickness, and source-to-detector distance. The results of these tests and a comparison of the results to the model predictions follow.

### 3.1 Experimental Apparatus

A circumstance that made it necessary to use source-to-detector distances much shorter than those employed on the actual rocket was that a large amount of scattering comes from the steel walls of even a 60-foot diameter vacuum sphere when the gauge is tested in the center of such a sphere. This was the experimental arrangement used by Giannini to calibrate the gauges (see Refs. 1 and 2). The response to multiple scattering down the vehicle walls represents about 0.4 percent of the response to the density of standard air and the scattering from the steel vacuum sphere walls in a 60-foot diameter vacuum sphere represents about 25 percent of the response to the density of standard air. This means that the response to multiple scattering down the vehicle walls would at best be only 1.6 percent above the constant response due to scattering from the vacuum sphere walls if the same experimental arrangement used by Giannini were used. It is obvious from this that the signal-to-noise ratio had to be improved.

Several design changes were employed to improve the signal-to-noise ratio. First the prototype was collimated to  $60^\circ$  in one plane ( $\pm 30^\circ$  from a vertical line perpendicular to the axis) and  $65^\circ$  in the other plane ( $45^\circ$  and  $110^\circ$  with respect to the axis) so that it could be placed on the floor of the vacuum sphere rather than in the center. The  $45^\circ$  and  $110^\circ$  angles were identical with those in the flight test gauges. Beaming the  $60^\circ$  angle to the sphere top means that scattering from the sphere walls would have to travel a total distance about twice that of the center-mounted case. This gives an increase in the signal-to-noise ratio of about a factor of 4 (i.e., reciprocal of source-to-detector distance squared). A second technique was to decrease the source-to-detector distance. Source-to-detector distances of 14.21 cm and 10.40 cm were used rather than the 42.23 cm previously used on the rocket-mounted gauges. This gives increases in the signal-to-noise ratio of factors of about 9.2 and 17.2. The overall increase in the signal-to-noise ratio using both techniques would be about 36 and 69. It was believed (and later borne out by the experimental results) that this would give adequate sensitivity.

The prototype gauge was constructed as shown in Fig. 1A and Fig. 1B. The main body of the gauge which was machined (mostly by hand) from lead bricks is shown in Fig. 1A. Fig. 1B is a cross-sectional view along the main axis of the gauge and shows the relation of the various parts of the gauge. The main features of the gauge are: (1) a rectangular hole down the axis of the lead body for a source holder guide, (2) two holes (three were originally used) machined to total angles

of  $60^\circ$  in one plane and  $65^\circ$  in the other plane as discussed earlier, (3) a commercial 2" X 2" NaI(Tl) crystal, photomultiplier tube, and preamplifier mounted at one end of the gauge, (4) a rack and pinion with a reversible dc electric motor for positioning the source under each of the two collimated holes, (5) three layers of fiberglass skin, constructed of the same material as the skin of the Nike-Apache Rocket, and (6) three concentrically-mounted shafts driven separately by three reversible dc electric motors for moving the fiberglass walls on and off of the main gauge body. The fiberglass walls were heat formed on a special brass mold that was machined to the same dimensions as the lead body of the gauge.

One problem occurred which required special attention. The commercial NaI(Tl) crystal, photomultiplier, and preamplifier unit had an offset as shown in Fig. 1B. This necessitated making one end of the lead gauge body slightly larger than the outside dimensions of the crystal in order for the fiberglass walls to fit snugly on the gauge body at all points. This presented no experimental problem, but made a correction of the mathematical model predictions necessary since the models were derived for a different geometry. This correction is discussed in the next section.

The final prototype gauge was capable of remotely positioning a source in either of two positions (representing source-to-detector distances of 5.59 and 4.09 in, or 14.21 cm and 10.40 cm) and three fiberglass walls thicknesses of 1/8, 1/4, and 3/8 inches, or 0.32, 0.64, and 0.95 cm, respectively. Four sources ( $^{241}\text{Am}$ ,  $^{153}\text{Gd}$ ,  $^{57}\text{Co}$ , and  $^{144}\text{Ce}$ ) of the same physical dimensions and which had to be changed manually were used. The gauge was placed in the bottom center of the 60-foot diameter vacuum sphere at the NASA-Langley Research Facility for the tests. A complete set of gauge responses to density and wall thickness for both source positions for one source could be completed in a period of 6 to 8 hours.

Since the model predictions had indicated that 90 percent of the wall-streaming response was due to the lowest energy (0.134 Mev) gamma ray of the  $^{144}\text{Ce}$  source and in order to meet contract requirements, it was necessary to use sources that emit only low energy gamma radiation to test our predictions. Consequently, the  $^{241}\text{Am}$ ,  $^{153}\text{Gd}$ , and  $^{57}\text{Co}$  were chosen since the primary gamma rays emitted by any of these sources has an upper limit of 0.136 Mev. In addition, to check the specific prediction of the flight test results, a  $^{144}\text{Ce}$  source was also obtained. However, we were unable to obtain useful data with the  $^{144}\text{Ce}$  source because of the large amount of high-energy gamma rays inherent to the source and because only 2 1/8 inches of lead shielding was used to shield the direct transmission gamma rays in the prototype gauge. It was also found that the other three sources all contained high-energy

contaminants (or in the case of  $^{57}\text{Co}$  a low yield 0.700 Mev) gamma rays. The pulse-height spectra of these sources, however, showed that the contaminant gamma rays had intensities at least **3** orders of magnitude less than the primary, low-energy gamma rays.

### 3.2 Model Predictions

Model predictions were made with the basic model for calculating response to density and the model for calculating the response to wall streaming for all experimental cases. These models are described in Ref. 3. One complication was that these models were derived to describe a gauge with the detector having the same outside diameter as the end of the shield it is butted against. The actual experimental apparatus had to be constructed with a shield diameter (at the detector end) of 2.625 inches while the NaI(Tl) crystal had an outside diameter of 2 inches. The model predictions were made on the basis of a detector diameter of 2.625 inches and were corrected by multiplying each result by  $2/2.625$ . This assumes that the response of the gauge is directly proportional to the detector diameter which should be a good assumption, at least for the limited change in the diameter of from 2.625 to 2 inches.

The model predictions for all experimental cases are given in Table 1. These values are on the basis of the fractional number of source emissions that are detected. The discriminator settings used are from zero to infinity.

### 3.3 Calibration of Sources

One of the major unforeseen problems encountered was in the calibration of the radioisotope sources used in the program. Ordinarily one would set up the detection equipment at some known distance from the source, obtain the counting rate, and calculate the disintegration rate of the source by employing standard calculation procedures with the necessary reported values of detector efficiency and air absorption coefficients. A combination of phenomena contributed to difficulties in using this simple technique. The sources had intensities which made it imperative to monitor them at large distances so that reasonably low counting rates would be obtained and the radiation detection equipment would not saturate. Yet as the source-to-detector distance was increased in the laboratory more and more scattering from the floor, lab benches, and the surrounding air occurred. This scattering response is unwanted since the usual technique for source calibration is based on obtaining only those radiations that travel directly from the source to the detector without scattering. With sources of higher energy one could easily compensate for this air scattering by gamma spectrometry since the energy difference between an unscattered and a scattered gamma ray is large for original gamma rays of high energy. This technique could not be employed here because the original gamma-ray energies of interest are low and there is little energy difference between scattered and unscattered gamma rays in this case.

We arrived at a technique whereby we obtained the response at a fixed, large source-to-detector distance and then subtracted the response when a small shield (sufficiently large to eliminate all gamma rays that travel directly from the source to the detector) was placed between the source and detector. In effect this net response must be due solely to those gamma rays that travel directly from the source to the detector. (This technique was suggested by R. L. Ely, Jr.) This concept was sound enough in principle, but we found that if we employed this technique in the laboratory we ended up subtracting one very large number from another and the precision was poor. This was due to the fact that the scattered gamma rays from the concrete floor and other laboratory equipment made up the bulk of the total response. To minimize this effect, we mounted the source and detector on an atmospheric sampling tower so that the only scattering would be due to the surrounding air. This worked quite well and we were able to obtain good data at source-to-detector distances of 27 feet.

It should be pointed out that in this study we are interested in the "effective" source intensity which is defined here as the disintegration rate which leaves the

outer surface of the source. We do not get involved with source self absorption or the attenuation due to the source capsule because our calibration technique is a direct measure of the effective source intensity. The calculation procedure is quite simple. The source emission rate is simply the observed counting rate divided by the counting yield

$$I_o = R/Y \quad (3.3-1)$$

where  $I_o$  is the source emission rate,  $Y$  is the counting yield, and  $R$  is the observed counting rate. The counting yield is a function of the source-to-detector distance, the detector size and shape, the detector efficiency for a particular gamma-ray energy, and the amount of attenuation between the source and detector. The counting yield can be given as a function of the geometry factor  $F_G$ , air absorption factor  $F_A$ , and the detector efficiency factor  $F_E$  for the present case.

$$Y = F_G F_A F_E \quad (3.3-2)$$

The geometry factor is given by:

$$F_G = \frac{A}{4\pi D^2} \quad (3.3-3)$$

where  $A$  is the detector area normal to the source and  $D$  is the source-to-detector distance. We used a detector with a one inch radius and a source-to-detector distance of 27.0 feet. The geometry factor for this case is  $2.3815 \times 10^{-6}$ ,

The air absorption factor  $F_A$  is given by:

$$F_A = \exp(-\mu x) \quad (3.3-4)$$

where  $\mu$  is the total attenuation coefficient for the gamma-ray energy of interest in air in  $\text{cm}^2/\text{g}$  units and  $x$  is the density times the thickness of the air between the source and detector in  $\text{g}/\text{cm}^2$  units. For the 60-kev gamma ray from  $^{241}\text{Am}$ , the absorption coefficient in air is  $0.185 \text{ cm}^2/\text{g}$ . The density thickness of 27 feet of standard air is  $1.062 \text{ g}/\text{cm}^2$ . Inserting these values into Eq. 3.3-4 gives a value for  $F_A$  of 0.822.

The detector efficiency factor is given in the literature for standard detector geometries at various source-to-detector distances (see Ref. 4). For low energies and large source-to-detector distances the detector efficiency factor for 2" X 2" NaI(Tl) crystals is unity. This was the case for all of our experimental conditions.

All of our counting yields were calculated according to this scheme. In addition, half-life corrections were made to account for the decay of  $^{153}\text{Gd}$  and  $^{57}\text{Co}$  between the calibration time and the time of the sphere experiments.

The calibration data on the three sources is given in Table 2. Values are given for the effective emission rate and the activity in curies calculated for abundances of 0.40, 0.46, and 0.98 for  $^{241}\text{Am}$ ,  $^{153}\text{Gd}$ , and  $^{57}\text{Co}$ , respectively. These activities can be compared to the nominal values reported by the supplier. It is found that, as one would expect, there is a significant amount of source self absorption. The nominal amount of  $^{153}\text{Gd}$  appears to be in error.

Our calibration results were taken with the same detection system that was employed in our prototype gauge. This procedure insures that a minimum of bias is introduced by detection system differences. The calibration spectra are given in Figs. 3, 4, and 5.

It is appropriate at this time to describe the techniques used generally in this study for calibrating pulse-height spectra and determining the frequency or counting rate between two arbitrary gamma-ray energies. The calibration technique is a standard one used in gamma-ray spectroscopy. It consists of obtaining the spectra of two or three known gamma-ray energies and identifying the channel number to the nearest 0.1 of a channel that each photopeak falls into. Then a plot on linear graph paper is made of gamma-ray energy versus the channel number in which the photopeak of that gamma-ray falls into. The equation of the best straight line through the experimental points represents the calibration for the particular set of radiation detection system parameters being used. In some cases in the present study, such as when obtaining  $^{144}\text{Ce}$  spectra, the known gamma-ray energies contained in each spectra can be used for calibration. In other cases small calibration sources of known energies must be used immediately before or after the spectrum of interest has been taken. The frequency of such calibrations naturally depends upon how stable the radiation detection system is.

The technique used for determining the frequency of counts within a given gamma-ray energy range essentially consists of the linear interpolation of counts between channels on either side of the appropriate fractional channel. The technique is best explained by use of an actual example. Suppose it is desired to integrate the counts lying between the gamma-ray pulse-height energies of 100 Kev and 200 Kev of a particular spectrum. Assuming that the linear calibration relation appropriate to that spectrum has been determined by the technique discussed in the previous paragraph, the channel numbers equivalent to 100 Kev and 200 Kev are

calculated to the nearest 0.1 of a channel. Suppose the channel numbers so calculated are 10.1 and 19.8. The counts in channels 12 through 19 are summed along with 0.9 of the counts in channel 11 and 0.8 of the counts in channel 20. The rule for the lowest energy channel is therefore to add one minus the fractional channel times the counts in the next higher channel. The rule for the highest energy channel is to add the fractional channel times the counts in the next higher channel. **This** technique has been used throughout in this study.

### 3.4 Experimental Results

The experimental data was taken with the previously described prototype gauge (see Figs. 1 and 2) connected to a Nuclear Chicago Model 186 high voltage supply and a Nuclear Data Model 120 multichannel analyzer with typewriter and oscilloscope readouts. One minute counts were taken and typed out for each set of experimental conditions. A total of 128 channels was used in every case. Gain shift was monitored by the position of the very low intensity, high energy gamma-ray peaks that were present in each of the sources and by occasionally counting standard high energy sources such as  $^{137}\text{Cs}$ ,  $^{60}\text{Co}$ ,  $^{133}\text{Ba}$ , and  $^{144}\text{Ce}$ .

We were unable to obtain useful data with the  $^{144}\text{Ce}$  source because of the large amount of high-energy gamma rays inherent in the source and because only 2 1/8 inches of lead shielding was used to shield the detector from gamma rays traveling directly from the source to the detector. These two factors caused a very high background response for this source.

Although we originally planned a third source-to-detector distance of about 6 cm, we had to abandon this position to add additional shielding between the source and detector. This change was necessary in order to reduce the direct transmission radiation to an acceptable level. Other experimental difficulties were encountered including shorting of the signal due to electrical breakdown of standard connectors inside the vacuum sphere. These problems resulted in a poor first set of data. However, all problems were corrected and the tests repeated. The next set of data was quite good and is reported here. This set of data is given in Table 3.

The data given in Table 3 was used to calculate net experimental responses to density and to each wall thickness for each source-to-detector distance and each of the three sources. All data was examined to see if any significant response was present from energies above the primary energies of each source. A negligible response was found above 60, 100, and 125 Kev for the sources  $^{241}\text{Am}$ ,  $^{153}\text{Gd}$ , and  $^{57}\text{Co}$ , respectively. The data reported are the counting rates in the energy ranges from 0 to 60 Kev, 0 to 100 Kev, and 0 to 125 Kev for the source  $^{241}\text{Am}$ ,  $^{153}\text{Gd}$ , and  $^{57}\text{Co}$ , respectively.

### 3.5 Comparison of Experimental Results with Predicted Values

To compare the experimental results with the model predictions, the model predictions given in Table 1 divided by 6 are multiplied by the effective emission rates reported in Table 2. The resulting model predictions are reported in Table 4 and compared directly with the net experimental counting rates that are derived from Table 3. The experimental gross response of each source to density at each source-to-detector distance is shown in Figs. 6, 7, and 8. The net experimental responses to wall thickness are shown for each source and each source position and compared to the model predictions in Figs. 9, 10, and 11.

Examination of the ratios of experimental to predicted values given in Table 4 indicates that our predictions for the gauge response to density were quite good. This was especially true at the larger source-to-detector distance where the ratios are 0.918, 0.996, and 1.001 for  $^{241}\text{Am}$ ,  $^{153}\text{Gd}$ , and  $^{57}\text{Co}$ , respectively. Even the predictions at the closer source-to-detector distance of 0.645, 0.726, and 0.739 are quite acceptable. This verification of the basic model predictions gives us confidence in the basic model and consequently, in our interpretation of the wall-streaming model which is similarly constructed.

The wall streaming experimental results, as we had expected, are much higher than the values predicted by our model which we know represents a minimum prediction. The ratios of experimental to predicted values given in Table 4 are directly analogous to buildup factors used in radiation transport calculations for shielding. We can apply this buildup factor in the present case by the following relation:

$$(I/I_o)_A = B(I/I_o)_M \quad (3.5-1)$$

where  $(I/I_o)_A$  is the actual ratio of detected radiations by wall streaming to the effective emission rate of the source,  $(I/I_o)_M$  is the model predicted ratio of detected radiations by wall streaming to the effective emission rate of the source, and B is the buildup factor or ratio of experimental to predicted response. The buildup factor B is obviously a function of source-to-detector distance, wall thickness, and source energy. It is also a function of the discriminator settings used on the radiation detection system. The reported values have no discriminator settings (or settings of zero and infinity). This means that the reported values would be somewhat lower if discriminators were employed. The values of B can be calculated for any arbitrary discriminator values from our data. It should be noted that the same discriminator settings would have to be employed on the responses

to density to obtain realistic values. Recall that the model predictions correspond to the case of no discriminator settings.

The major question to be answered here is whether or not the multiple scattering of gamma rays down the rocket wall could account for all or most of the high background reported in Refs. 1 and 2 for the previous rocket tests of prototype gauges. This cannot be answered directly from experimental results since our prototype gauge necessarily employed source-to-detector distances much smaller than that employed in the rocket-mounted prototypes. However, it is generally accepted that buildup factors increase with increasing relaxation lengths and source-to-detector distance is directly related to relaxation length in the present case. The buildup factors reported here support this statement in 7 of the 9 cases reported and the two cases which do not support it are for the sources with lowest energies at the largest wall thicknesses. For the experimental case with parameters closest to the rocket-mounted prototypes, a buildup factor of 8.73 is observed. Since we previously predicted about 27.2 percent of the observed background response was due to multiple scatter down the rocket walls, insertion of these values into Eq. 3.5-1 indicates that this phenomenon would actually predict about 2.4 times more background than was actually obtained. Even though this estimate should be decreased somewhat because discriminator settings were employed on the rocket-mounted tests, it is obvious that the experimental results confirm our hypothesis that the multiple scattering of the primary gamma rays down the rocket wall accounts for the bulk of the background response observed in the prototype rocket tests. We have not determined the effect of discriminator settings on the buildup factor since we were unable to use a  $^{144}\text{Ce}$  source and the equivalent settings for other source energies are not directly related to those employed with the  $^{144}\text{Ce}$  source. Our findings do indicate that no major changes in the buildup factor would occur--certainly the changes would be less than a factor of two which would still confirm our hypothesis.

Another objective of the present program was to determine the factors necessary to correct our mathematical model predictions. In effect, this consists of determining the buildup factors for the multiple scattering wall streaming model as defined by Eq. 3.5-1 since the experimental correspondence with the basic model predictions was acceptable. This objective was seriously hampered by our inability to obtain data at three source-to-detector distances. However, at best we would have obtained data only in the range of source-to-detector distances from about 6 cm to 14.21 cm which is still quite far from the 42 cm employed previously and the even greater distances that may be desirable in future gauge designs. (It should

be pointed out that this was not due to poor planning on our part, but rather to the experimental limitation imposed by significant amounts of scattering from available vacuum sphere walls. This was discussed in Sec. 3.1.) The buildup factor was found to be a complex function of **all** three parameters: source energy, wall thickness, and source-to-detector distance. Because of this the factor could not be generally determined with the limited amount of data available by using simple correlations. However, the amount of data obtained is quite sufficient for checking a more sophisticated model of the wall streaming. ~~We~~ therefore suggest that a more sophisticated model be developed for the next phase of this program. Monte Carlo techniques would be particularly appropriate for this. ~~We~~ would anticipate developing a Monte Carlo program for calculating buildup factors over the range of conditions of interest. The results of this program would be used to develop simple engineering correlations which could easily be used in optimum design programs.

### 3.6 Conclusions

In summary, it is first concluded that multiple scattering of the primary, low-energy gamma rays down the rocket walls does account for the major part of the previously unexplained high background response observed in the two flight tests as was our contention. However, the second conclusion is that the factor necessary for correcting our model predictions of multiple wall scattering cannot be generally determined from the limited experimental data taken.

#### 4. Experimental Verification of Model Predictions Regarding Shielded Source

One of the surprising results of the second rocket test program (see Ref. 2) was that the response to density with a small tungsten cup shielding the source was only reduced to about 1/3 of that when the cup was not shielding the source. In addition, the background response of the source when the shielding was in place was actually slightly higher than when the source was unshielded. It was the purpose of this program to quantitatively study this phenomenon by taking experimental direct-transmission gamma-ray spectra around a similar gauge and use this data as input to our mathematical models to predict the response with the tungsten shield on and off the  $^{144}\text{Ce}$  source. A comparison of these predicted values to those actually obtained in the flight test would be another test of the ability of the mathematical models to predict and explain actual gauge response.

#### 4.1 Experimental Apparatus

The experimental apparatus used in this program was a "back-up" model of the rocket-mounted gauge actually used in the flight test complete with a small Calibration source of  $^{144}\text{Ce}$  that was constructed with the same self-absorption characteristics as the actual full-size  $^{144}\text{Ce}$  source used in the flight test. The strength of the  $^{144}\text{Ce}$  source used in these experiments was 0,054 curies when the tests were made. In addition we used the same radiation detection equipment (NaI crystal, photomultiplier, preamplifier, high voltage supply, and multichannel analyzer) described previously in Sec. 3.1. A power supply was furnished by Langley Research Center to actuate the tungsten cup shield and hold it in either the on or off position.

The experimental spectra were taken in a large building at the Langley Research Center with the rocket mounted about 3 feet off the concrete floor in a horizontal position. The NaI(Tl) crystal was rotated about the source position at a distance of 15 feet from the rocket and at the same distance (about 3 feet) above the concrete floor as the source. A sketch showing a plan view of the experimental test geometry is given in Fig. 12.

## 4.2 Experimental Results

Gamma-ray spectra were obtained using the same technique as that used for calibrating the low energy sources described in Sec. 3.3 at  $15^\circ$  intervals from  $15^\circ$  to  $165^\circ$  around the source with the tungsten cup on and off the source. Since the concrete floor scattered a great deal of the emitted gamma rays into the detector our experimental data were somewhat erratic due to subtracting one large number from another. Better data would have been obtained if the rocket-mounted gauge and detection system were suspended in air, but we decided not to use this refinement since it would entail a great deal more experimental effort. Two typical spectra at  $90^\circ$  from the rocket axis with the tungsten shield on and off are shown in Fig. 13.

There are two surprising qualitative conclusions that are evident from all the shielded versus unshielded spectra results. The first of these is that the unshielded spectra are almost always higher (100 cases out of 110) than the shielded spectra over all gamma-ray energies for a given position. We expected to find that the shielded spectra would be consistently higher than the unshielded spectra in the gamma-ray energy range from 134 Kev up to about 500 Kev. This would have indicated that more bremsstrahlung was being produced in that energy range with the shield over the source. The actual results indicate that this was not the case and that the primary production of bremsstrahlung is within the source and source capsule rather than in the tungsten cup. This indicates that the source is relatively thick compared to the range of 3-Mev beta particles in cerium. It also obviously indicates that the background response being higher for the shield closed position cannot be explained on the basis of greater bremsstrahlung production when the source is shielded by the tungsten cup. It is likely that this phenomenon was due to a simpler explanation such as the time period available for counting with the source shielded being slightly longer than that with the source unshielded.

The second surprising conclusion is that the relative amounts of 134-Kev gamma rays to the amounts of 694-Kev and 2,180-Kev gamma rays are much lower than the published abundance values indicate by a factor of  $1/2$  or  $1/3$ . This means that the 134-Kev gamma rays undergo more self-absorption than was previously thought and that the responses predicted from the high-energy gamma rays in Ref. 3 should be relatively larger for both the background response and the response to density. This result is also probably due to the source being quite thick. It should be noted that both of these qualitative conclusions are based on the assumption that the small calibration source used in the present study has the same self-absorption properties as the larger flight source.

The experimental results of the present study were derived from the individual pulse-height spectra taken at  $15^\circ$  intervals from  $15^\circ$  to  $165^\circ$ . The spectra were first calibrated by establishing the channel numbers to the nearest 0.1 of a channel in which the three high-energy gamma-ray photopeaks fell. Then the Calibration technique outlined in Sec. 3.3 was performed on each spectra to determine the linear relationship between channel number and gama-ray pulse-height energy. Then the counts per minute in various energy ranges varying from 90 Kev to 2300 Kev were determined by the spectrum integration technique described in Sec. 3.3. These derived results are listed in Table 5.

### 4.3 Model Predictions

Model predictions were made with both the basic model and the wall-streaming model described in Ref. 3 for a range of maximum and minimum integration angles and a range of gamma-ray energies. This is necessary so that the experimental spectra results can be used to numerically integrate over all possible angles and gamma-ray energies. This integration is described in the next section. A total of 60 model predictions were run with each model covering 6 increments of angular integration from 10 to 170° and 10 gamma-ray energies from 100 to 2000 Kev. These calculations were all made for a lower discriminator setting of 90 Kev and an upper discriminator setting of 155 Kev as were used in the flight test gauge. All other conditions of the flight gauge were used appropriately in the models.

One complication arises in the use of our existing models for direct application in the present case. The existing models were derived for isotropic sources and the parameter actually calculated by the models is the detected number of gamma rays of a particular energy that are originally directed within prescribed angular limits divided by the total number of gamma rays emitted at all angles from the surface of the source of that energy. In the present case we will determine the actual distribution of gamma rays from the source at all energies and this distribution will not be isotropic. We will therefore need model predictions that are defined as the detected number of gamma rays of a particular energy that are originally directed within prescribed angular limits divided by the total number of gamma rays emitted from the surface of the source of that energy that are originally directed within the prescribed angular limits. The isotropic prediction of  $(I/I_o)_i$  can be corrected to the required non-isotropic prediction  $(I/I_o)_n$  by multiplying the isotropic prediction by the ratio of the total number of gamma rays emitted at all angles to the number of gamma rays emitted within the prescribed angular limits of interest.

$$(I/I_o)_n = \frac{(I/I_o)_i \int_0^{\pi} \frac{\sin \phi}{2} d\phi}{\int_{\phi_{\min}}^{\phi_{\max}} \frac{\sin \phi}{2} d\phi} \quad (4.3-1)$$

Where  $\phi_{\min}$  is the prescribed minimum angle and  $\phi_{\max}$  is the prescribed maximum angle.

We know that

$$\int_0^{\pi} \frac{\sin \phi \, d\phi}{2} = 1 \quad (4.3-2)$$

Therefore Eq. 4.3-1 reduces to:

$$(I/I_o)_n = \frac{(I/I_o)_i}{\int_{\phi_{\min}}^{\phi_{\max}} \frac{\sin \phi \, d\phi}{2}} \quad (4.3-3)$$

The non-isotropic predictions are reported in Table 6. They were obtained from the isotropic predictions and corrected for the appropriate angular limits according to Eq. 4.3-3.

#### 4.4 Comparison of Experimental Results with Predicted Values

To predict the gauge response to density and wall streaming one must integrate over all possible energies and angles the product of : (1) the predicted number of detected gamma rays of a given energy and original direction per unit number of gamma rays emitted of that energy and direction and (2) the number of gamma rays emitted from the source of that energy and direction. Mathematically stated this is:

$$R = \int_{E=0}^{E_{\max}} \int_{\phi=0}^{\phi_{\max}} F(\phi, E) N(\phi, E) d\phi dE \quad (4.4-1)$$

where R is the predicted response,  $F(\phi, E)$  is the predicted fractional number of gamma rays detected of energy E and emitted angle  $\phi$ , and  $N(\phi, E)$  is the total number of gamma rays emitted within the energy range E to E + dE within the angular range  $\phi$  to  $\phi + d\phi$ . Equation 4.4-1 can be put into the following form:

$$R = \int_{E=0}^{E_{\max}} \left[ \int_{\phi=0}^{\phi_1} F(\phi, E) N(\phi, E) d\phi + \int_{\phi_1}^{\phi_2} F(\phi, E) N(\phi, E) d\phi + \dots \right. \\ \left. + \dots \int_{\phi_{n-1}}^{\phi_n} F(\phi, E) N(\phi, E) d\phi \right] dE \quad (4.4-2)$$

where  $\phi_n = \phi_{\max}$ .

Assuming that the number of  $\phi$  intervals (n) can be chosen so that  $F(\phi, E)$  and  $N(\phi, E)$  are essentially constant and independent of  $\phi$  within each small interval gives:

$$R = \int_{E=0}^{E_{\max}} [F(\bar{\phi}_1, E) N(\bar{\phi}_1, E) (\phi_1 - \phi_0) + F(\bar{\phi}_2, E) N(\bar{\phi}_2, E) (\phi_2 - \phi_1) + \dots \\ \dots + F(\bar{\phi}_n, E) N(\bar{\phi}_n, E) (\phi_n - \phi_{n-1})] dE \quad (4.4-3)$$

where  $\bar{\phi}_1$  is the arithmetic average of  $\phi_0$  and  $\phi_1$ . Equation 4.4-3 can be expressed as:

$$R = \int_{E=0}^{E_{\max}} \sum_{i=1}^{i=n} F(\bar{\phi}_i, E) N(\bar{\phi}_i, E) (\phi_i - \phi_{i-1}) dE \quad (4.4-4)$$

Similarly the total energy range can be split into intervals.

$$R = \int_{E=0}^{E_1} \sum_{i=1}^{i=n} F(\bar{\phi}_i, E) N(\bar{\phi}_i, E) (\phi_i - \phi_{i-1}) dE + \dots \int_{E_{m-1}}^{E_m} \sum_{i=1}^{i=n} F(\bar{\phi}_i, E) N(\bar{\phi}_i, E) (\phi_i - \phi_{i-1}) dE \quad (4.4-5)$$

where  $E_m = E_{\max}$ . Assuming that the number of E intervals (m) can be chosen so that  $F(\bar{\phi}_i, E)$  and  $N(\bar{\phi}_i, E)$  are essentially constant and independent of E within each small interval gives:

$$R = \sum_{j=1}^{j=m} \sum_{i=1}^{i=n} F(\bar{\phi}_i, \bar{E}_j) N(\bar{\phi}_i, \bar{E}_j) (\phi_i - \phi_{i-1}) (E_j - E_{j-1}) \quad (4.4-6)$$

where  $\bar{E}_j$  is the arithmetic average energy in the energy interval from  $E_{j-1}$  to  $E_j$ . We know that  $F(\bar{\phi}_i, \bar{E}_j)$  is simply  $(I/I_0)_n$  as defined in Sec. 4.3 for gamma-ray energy  $\bar{E}_j$  and the angular interval from  $\phi_{i-1}$  to  $\phi_i$ .

The values given in Table 5 are the number of counts per unit time in various gamma-ray pulse-height energy intervals at a distance of 15 feet at a particular angle. Therefore, the values in Table 5 represent the number of counts per unit time in various pulse-height ranges per unit solid angle at solid angle  $\Omega$ . If we denote gamma-ray pulse-height energy by e, then the values of Table 5 are denoted  $N(\Omega[\phi], \bar{e}_j) (e_j - e_{j-1})$ . These values are averaged over various  $\phi$  intervals and reported in Table 7. These values are denoted  $N(\Omega[\bar{\phi}_i], \bar{e}_j) (e_j - e_{j-1})$ , where  $\bar{\phi}_i$  is the average  $\phi$  in the interval  $\phi_i$  to  $\phi_{i-1}$ .

One must obviously convert from gamma-ray pulse-height spectra to actual gamma-ray spectra. To accomplish this one must know the relationship between gamma-ray energy and the resulting distribution of pulse-height energies. An approximate relationship is used in the present study. This relationship is graphically shown in Fig. 14 where the frequency of counts per unit energy is plotted versus gamma-ray pulse-height energy. The pulse-height spectrum shown is for a single gamma-ray with an energy equivalent to the pulse-height energy at the center of the photopeak. This same distribution was assumed for purposes of assigning detector efficiencies in the mathematical models (see Ref. 3).

A pertinent characteristic of the spectrum shown in Fig. 14 is that:

$$A_P + A_C = 1 \quad (4.4-7)$$

where  $A_P$  is the area under the photopeak portion of the spectrum and  $A_C$  is the area under the Compton continuum portion of the spectrum. The energy  $T_{\max}$  is the maximum Compton beta particle energy from an original gamma-ray energy E. It is

given by :

$$T_{\max} = \frac{2 E^2}{E + 0.511} \quad (4.4-8)$$

where  $T_{\max}$  and  $E$  are in Mev units. Photopeak areas ( $A_p$ ) are given in Ref. 5 for many standard size crystals of NaI as a function of original gamma-ray energy. One can determine  $A_c$  from Eq. 4.4-7 and  $h$  can then be determined from:

$$A_c = h T_{\max} \quad (4.4-9)$$

Total intrinsic efficiencies,  $E_T$ , are also given in Ref. 5 for standard size crystals of NaI as a function of original gamma-ray energy. These efficiencies are defined here as the number of gamma rays detected per unit number of gamma rays that intersect the detector.

With these assumptions for the relation between pulse-height spectra and original gamma-ray energy, one can convert from pulse-height spectra to original gamma-ray spectra. This is accomplished by a spectrum stripping process in which the highest pulse-height frequency is converted to a gamma-ray frequency and the appropriate proportion of this highest energy is subtracted from all lower energies. Then the next highest energy is treated in similar fashion and so on until all energies have been stripped.

First the assumed pulse-height of the gamma rays with an average energy at the center of the upper energy interval given in Table 7 is appropriately split into 10 intervals. This is shown in Fig. 15. From data in Ref. 5 it is found that the photofraction or  $A_p$  for a gamma-ray energy  $E$  of 2180 Kev is 0.216. This means that  $A_c$  from Eq. 4.4-7 must be 0.784. By using Eq. 4.4-8,  $T_{\max}$  is found to be 1950 Kev. From Eq. 4.4-9,  $h$  is  $0.402 \times 10^{-3}$  per Kev. By proper integration one can determine the relative amount of the total pulse-height spectrum from a gamma-ray with an energy of 2180 Kev that is in each of the energy intervals shown in Fig. 15. The fraction in the top interval must be  $A_p$  plus the integrated amount in the Compton continuum from 1800 to 1950 Kev. This is simply  $0.216 + (0.402 \times 10^{-3})(1950 - 1800)$  or 0.276. Let us call these fractions  $G(e_i, e_{i-1}, E_j)$ ; where  $e_{i-1}$  is the lower boundary of the pulse-height energy interval,  $e_i$  is the upper boundary, and  $E_j$  is the gamma-ray energy interval. The number of gamma rays of energy  $E_1$  where 1 refers to the top size is given by:

$$N(\Omega [\bar{\phi}_i], E_1) (E_1 - E_o) = \frac{N(\Omega [\bar{\phi}_i], e_1) (e_1 - e_o)}{G(e_1, e_o, E_1) E_T(E_1)} . \quad (4.4-10)$$

Equation 4.4-10 converts the top energy interval from a pulse-height frequency to a gamma-ray frequency. To strip this top energy from all lower pulse-heights one subtracts the appropriate number of photons according to:

$$N(\Omega [\bar{\phi}_i], E_j) (E_j - E_{j-1}) = N(\Omega [\bar{\phi}_i], e_j) (e_j - e_{j-1}) - \frac{[N(\Omega [\bar{\phi}_i], E_1) (E_1 - E_o) - N(\Omega [\bar{\phi}_i], e_1) (e_1 - e_o)]}{G(e_j, e_{j-1}, E_1)} \quad (4.4-11)$$

This procedure is carried out for each subsequent highest energy interval. In the present case only the three top energies were stripped from the spectra. The values of  $G(e_j, e_{j-1}, E_j)$  and  $E_T(E_j)$  that were used are given in Table 8. Table 9 gives the values of  $N(\Omega [\bar{\phi}_i], E_j) (E_j - E_{j-1})$  obtained by stripping the three highest energy intervals from the spectra of Table 7.

To convert the values of Table 9 to the required  $N(\bar{\phi}_i, \bar{E}_j) (E_j - E_{j-1}) (\phi_i - \phi_{i-1})$  one must use the definition of  $\Omega$ .

$$\Omega = 2\pi \sin \phi \quad (4.4.12)$$

Each value in Table 9 is multiplied by  $2\pi \sin \bar{\phi}_i^*$  to obtain  $N(\bar{\phi}_i, \bar{E}_j) (E_j - E_{j-1})$ . These values are then multiplied by  $(\phi_i - \phi_{i-1})$  and the resulting values of  $N(\bar{\phi}_i, \bar{E}_j) (E_j - E_{j-1}) (\phi_i - \phi_{i-1})$  are listed in Table 10.

The integration indicated by Eq. 4.4-1 is carried out according to the method indicated by Eq. 4.4-6 on the values in Table 6 and Table 10. The resulting individual products  $F(\phi_i, E_j) N(\bar{\phi}_i, \bar{E}_j) (\phi_i - \phi_{i-1}) (E_j - E_{j-1})$  are listed in Table 11. It is found that the total predicted responses to density with the shield open and closed are 0.10890 and 0.06241, respectively. The total predicted responses to wall streaming with the shield open and closed are  $1.458 \times 10^{-4}$  and  $1.118 \times 10^{-4}$ , respectively. The predicted ratio of shield open to shield closed response to density is 1.745 while the experimental ratio obtained in the rocket test was 3.0. Likewise, the predicted ratio of shield open to shield closed response to wall

\*\_\_\_\_\_

Since only relative numbers were required, the  $2\pi$  was omitted in the calculations.

streaming is 1.304 while the experimental ratio obtained in the rocket test was 0.920.

These predicted values indicate that the ratio of the shield open response to shield closed response to density was actually higher than one would expect while the ratio of the open to closed response to wall streaming was lower. We feel that in view of the many assumptions that had to be made to arrive at these predictions the results are quite good. Among these assumptions are: (1) that the small calibration source had self-absorption characteristics that were identical to the large flight test source, (2) that the sources were both symmetrical about the major gauge axis so that the experimental data that we took in one plane was representative, (3) that air absorption was negligible for all gamma-ray energies at a source-to-detector distance of 15 feet, (4) that enough detail was obtained by taking spectra at  $15^\circ$  intervals, and (5) that the simple technique employed to translate pulse-height spectra into gamma-ray spectra was sufficient. We do not suggest that these predictions be further refined since the first assumption must always be made. This assumption can never be verified since the original flight test source is no longer available.

In determining the flight test ratio of shield open to shield closed response to density for comparison with our results, a surprising result was found. The net response to density with shield open was not larger than the shield closed response by a constant factor. The ratio changed from about 1.8 to about 4.0 over the range of altitude from 0 to 55 Km. There is no theoretical reason why this should occur. One must conclude from this that the response of the radiation detection system or the alternator system varied during the flight.

By summing the gamma-ray frequencies for each angular interval from 10 to 170 degrees for each energy range given in Tables 10 and 11, the source of the predicted responses to density and wall streaming can be evaluated. Assuming that the energy interval from 90 to 160 Kev is representative of the 0.134-Mev gamma-ray frequency, 160 to 500 Kev is representative of the bremsstrahlung, and everything above 500 Kev is representative of the high-energy gamma rays, then the relative amounts contributed from these three sources for all cases studied can be evaluated. This has been done and the relative percentages are reported for all cases in Table 12. The most surprising result is that 57.3 percent of the total emitted from the source is from the high-energy gamma rays. A source with no self-absorption and no bremsstrahlung

would contain only about 15 percent high-energy gamma rays. This indicated that the source exhibited a large amount of self-absorption for the 0.134-Mev gamma ray and that a large amount of bremsstrahlung was generated in the source itself. The tungsten shield did not contribute significantly to the generation of bremsstrahlung as was previously thought.

#### 4.5 Conclusions

In view of the assumptions necessary and the inconsistency pointed out in the flight test data, the predicted ratios of 1.74 and 1.30 for shield open to shield closed response to density and wall streaming as compared to experimental values of 3.00 and 0.92 represent a reasonably good substantiation of the model predictions. Two surprising results are the very low number of 0.134-Mev gamma rays being emitted from the source and the lack of bremsstrahlung being generated by the tungsten cup. The explanation for these two results is that the source is much thicker than was thought and therefore exhibits a large amount of self-absorption for the 0.134-Mev gamma rays and is capable of generating essentially all of the beta-particle bremsstrahlung that is possible. The predicted relative contributions of 0.134-Mev gamma rays, bremsstrahlung, and high-energy gamma rays for all experimental cases are summarized in Table 12. For example, it is seen from Table 12 that 17.4 percent of the background with the shield open comes from 0.134-Mev gamma rays, 47.5 percent comes from bremsstrahlung, and 35.1 percent comes from the high-energy gamma rays. One should not lay too much stress on the absolute values given in Table 12 since the calculations used in translating pulse-height spectra into photon spectra were somewhat crude.

## 5. Recommendation for Continuation of Phase II

In Phase II of this program we are to adapt the cylindrically-symmetric models derived in Ref. 3 to three dimensional models and incorporate them into a program for determining an optimum gauge design. The decision to proceed with Phase II was to be based on whether or not the experimental results of Phase I verified the models that we had derived. We conclude that the experimental results do verify these models quite well and, therefore, we recommend proceeding with Phase II of the program. Since the buildup factor necessary for correcting our model predictions of wall streaming was too complex to determine generally by simple correlations with the limited amount of data that we took in Phase I, we suggest that a more comprehensive model of wall streaming be developed in Phase II. This model would probably be derived by Monte Carlo techniques.

## References

1. "Air Density Sensor ADS-103 Design and Operation," NASA Contractor Report on Contract No. NAS1-4349, Aug. 5, 1965.
2. D. B. Hakewessel, "Feasibility Study for an X-ray Backscatter Free Air Density Sensor," NASA Contractor Report No. 66148, Sept. 1966.
3. R. P. Gardner and D. R. Whitaker, "A Theoretical Study of the Gamma-ray Scattering Technique for Measuring Atmospheric Density," NASA Contractor Report No. 66142, Aug. 1966.
4. R. L. Heath, "Scintillation Spectrometry Gamma-Ray Spectrum Catalogue," AEC Research and Development Report IDO-16408, July 1, 1957.
5. C. E. Crouthamel, Applied Gamma-Ray Spectrometry, Pergammon Press, New York, 1960.

Fig. 1A. Isometric Drawing of the Main Body of the Prototyp<sup>a</sup> Gauge (Full Scale)

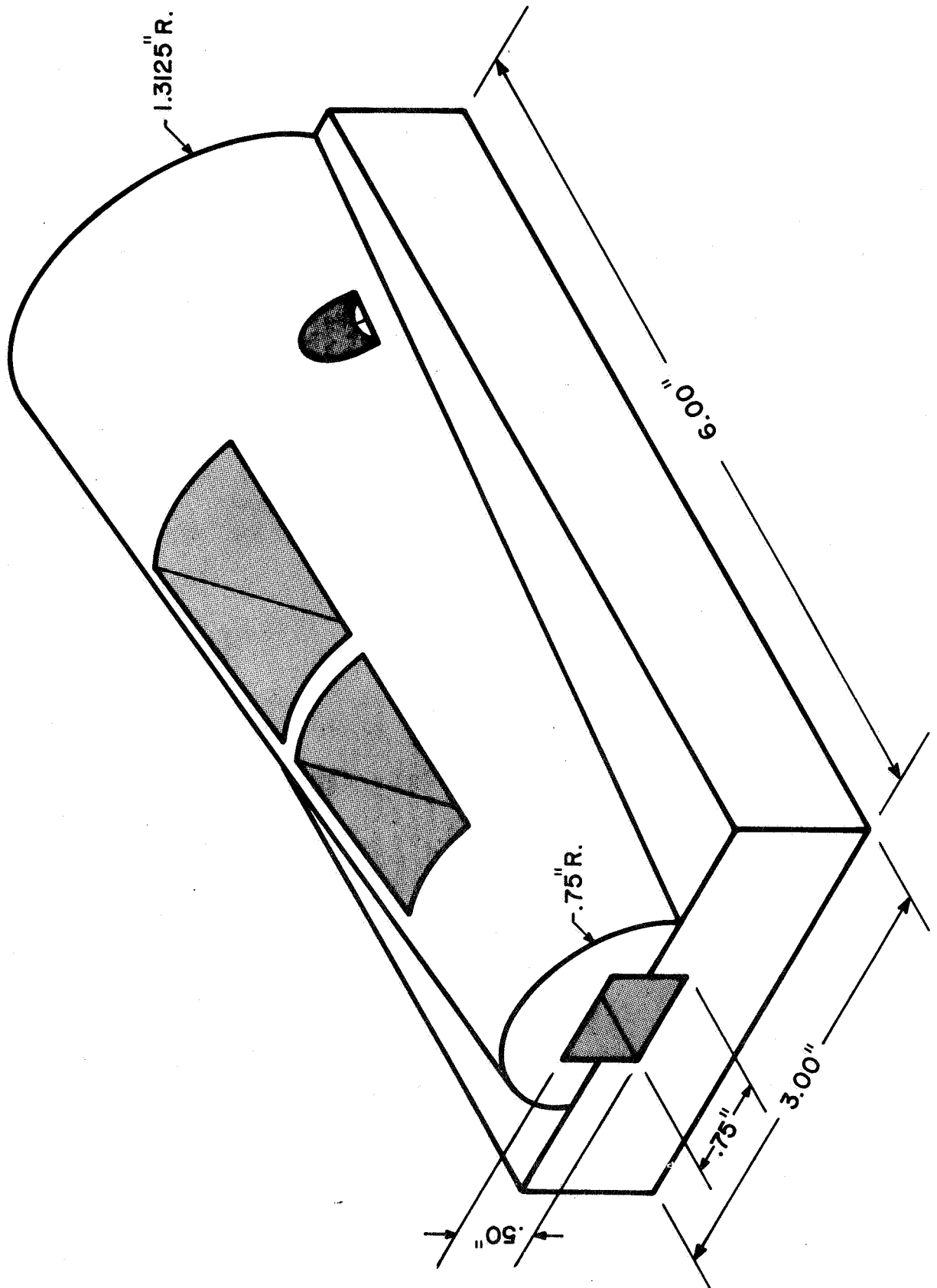


Fig. 1B. Cross-Sectional View of the Prototype Assembly (One-Half Scale)

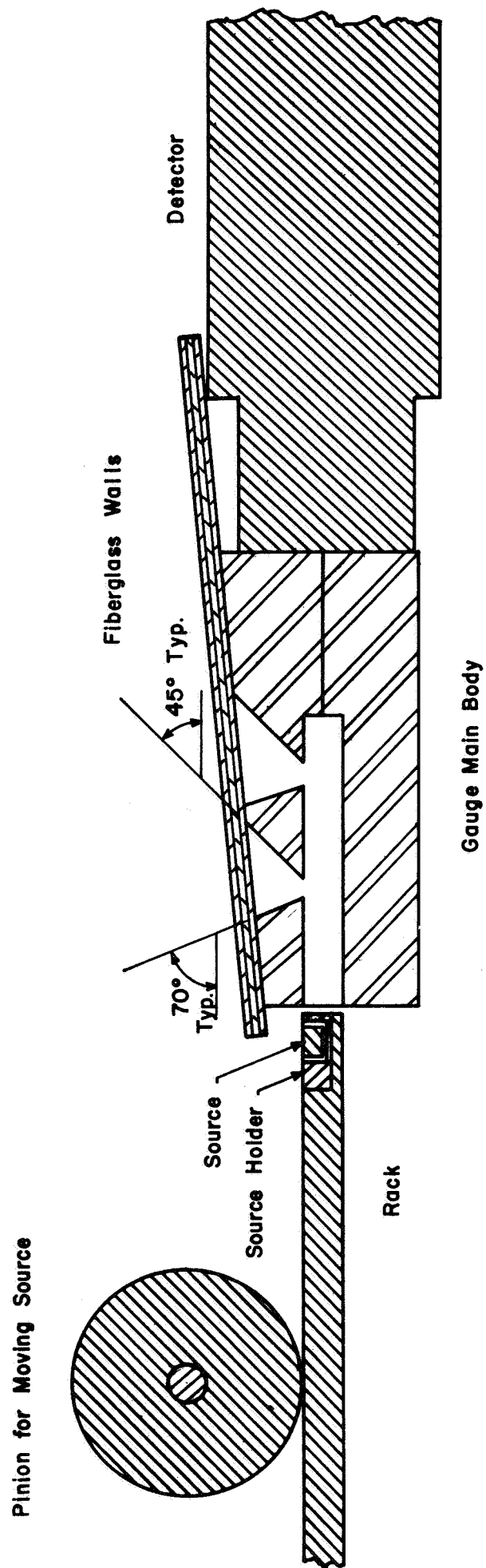
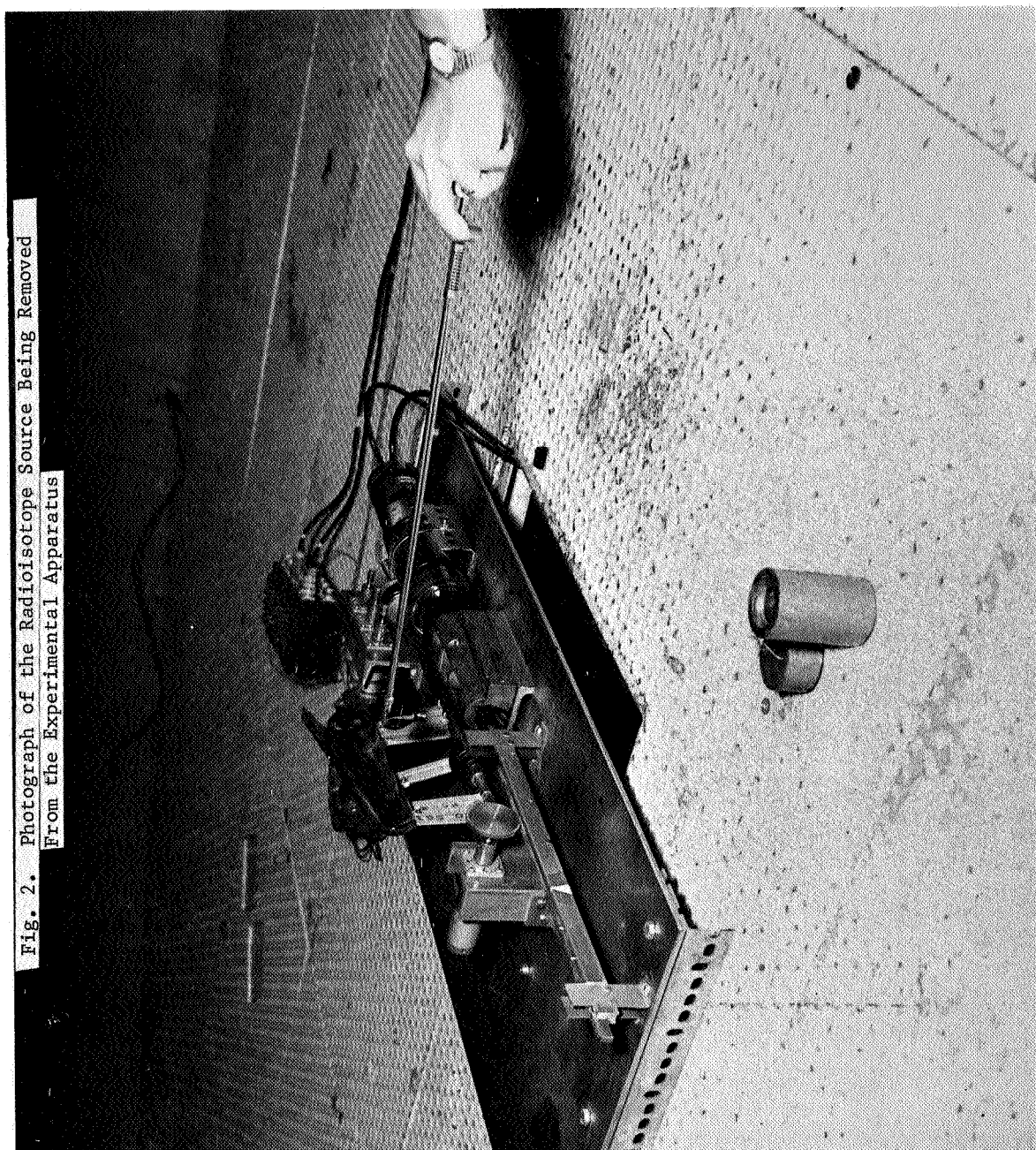


Fig. 2. Photograph of the Radioisotope Source Being Removed  
From the Experimental Apparatus



KE SEMI-LOGARITHMIC 46 6213  
5 CYCLES X 70 DIVISIONS MADE IN  
KEUFFEL & ESSER CO.

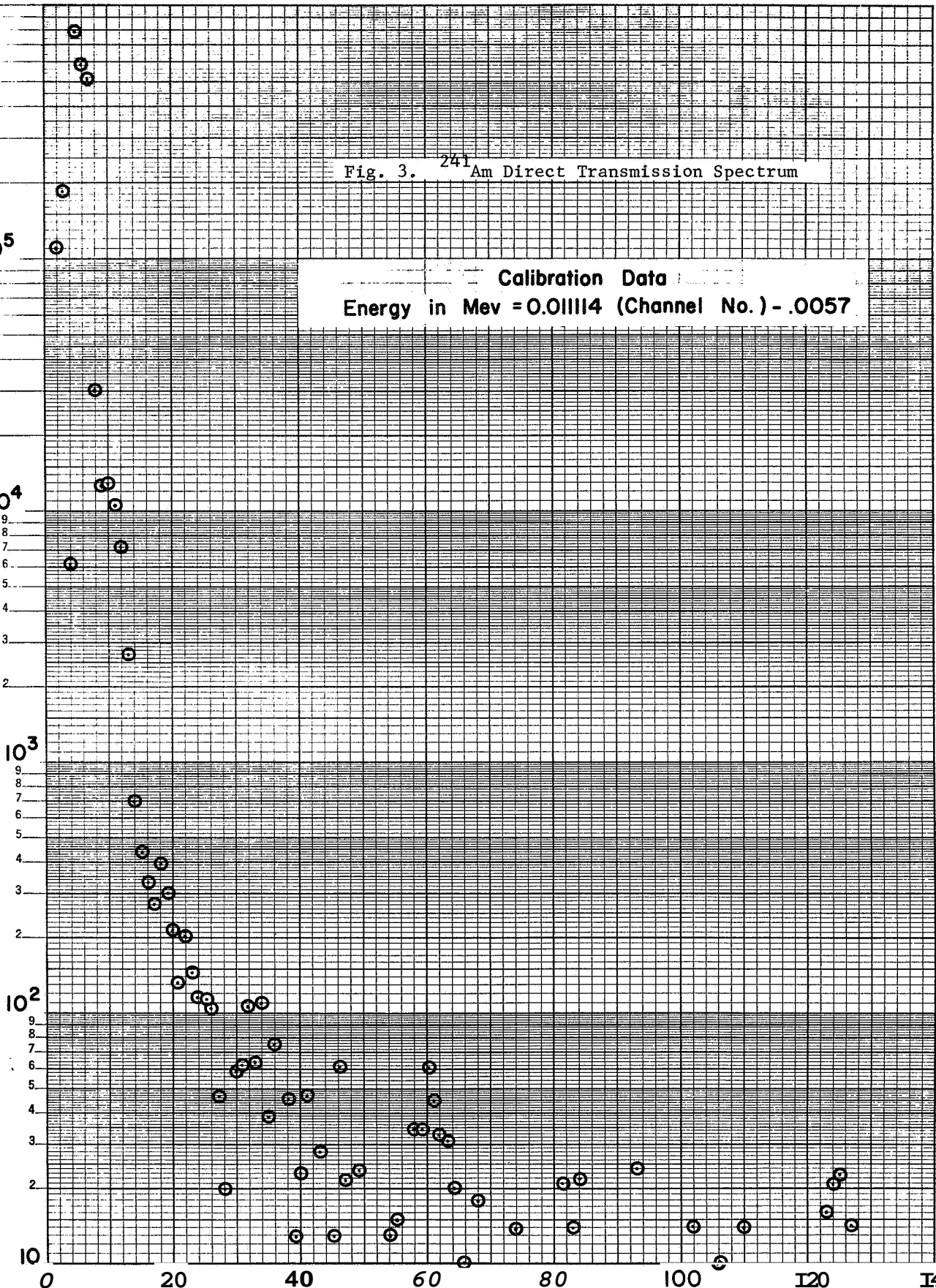
Net Counts/Min.

$10^6$

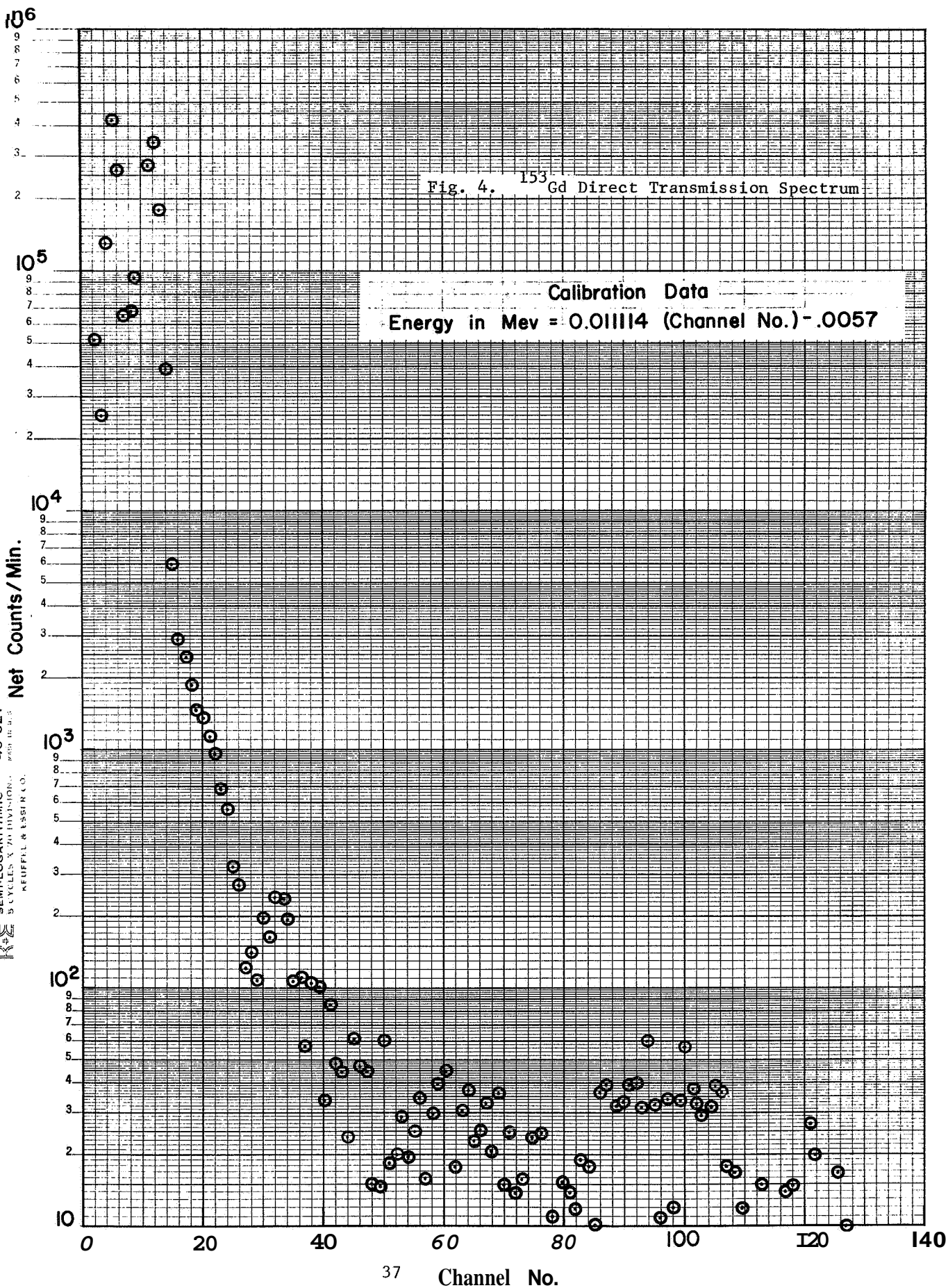
9  
8  
7  
6  
5  
4  
3  
2  
  
 $10^5$   
9  
8  
7  
6  
5  
4  
3  
2  
  
 $10^4$   
9  
8  
7  
6  
5  
4  
3  
2  
  
 $10^3$   
9  
8  
7  
6  
5  
4  
3  
2  
  
 $10^2$   
9  
8  
7  
6  
5  
4  
3  
2  
  
10

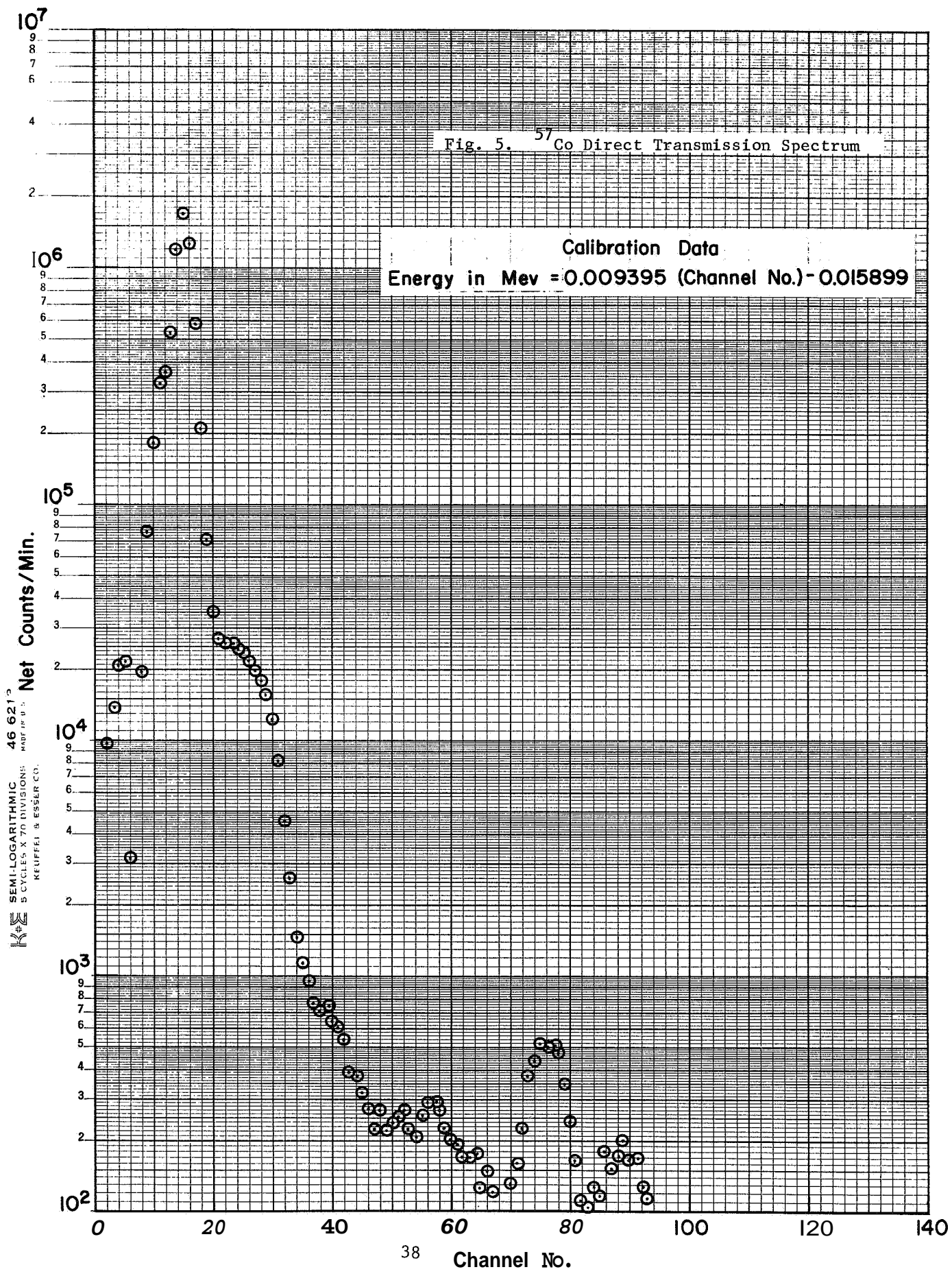
Fig. 3.  $^{241}\text{Am}$  Direct Transmission Spectrum


Calibration Data  
Energy in Mev =  $0.011114 (\text{Channel No.}) - .0057$

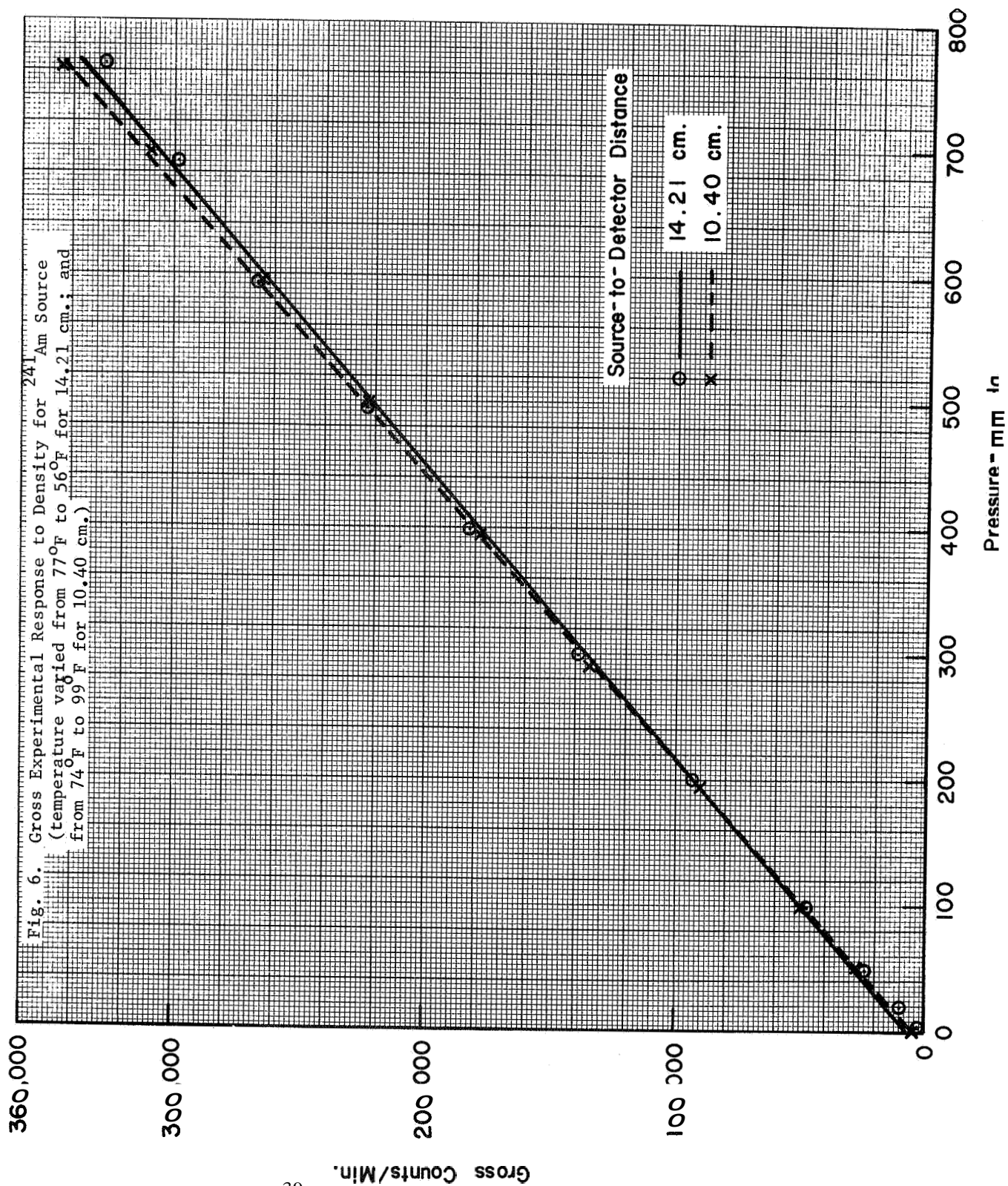


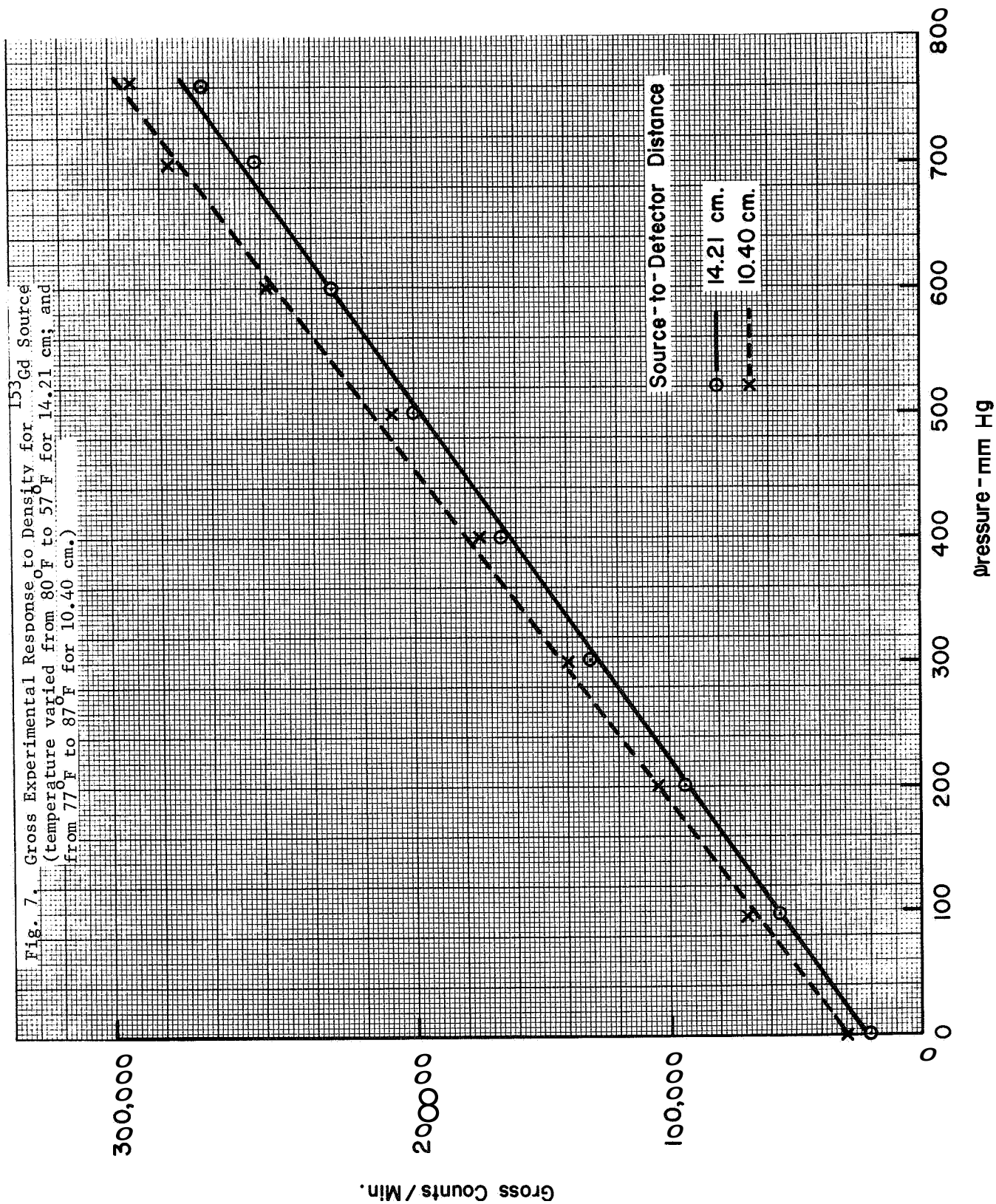
36 Channel No.





 SEMI-LOGARITHMIC 46 6213  
 5 CYCLES X 70 DIVISIONS  
 KEUFFEL & ESSER CO.





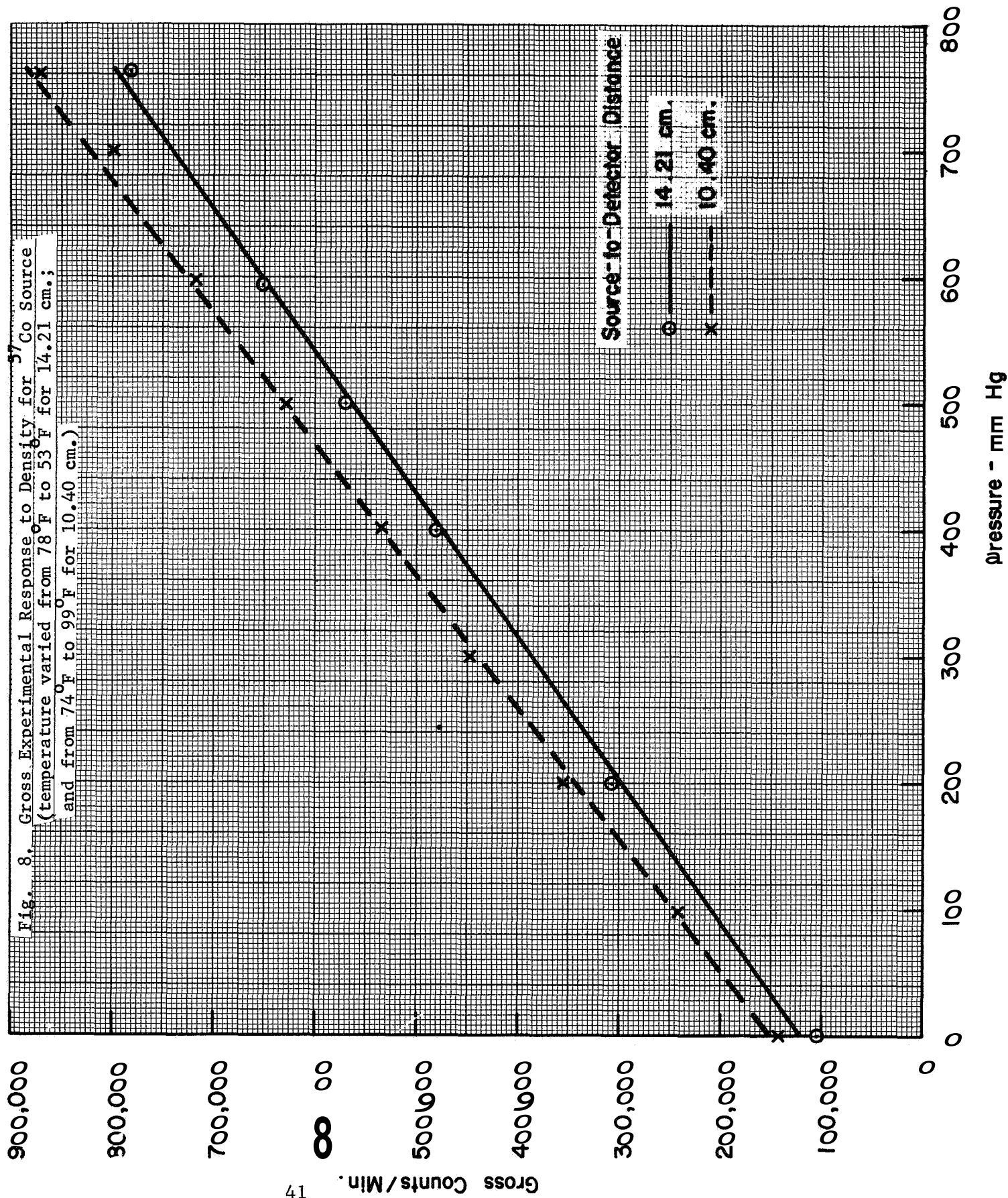


Fig. 9. Net Experimental Response and Predicted Response To Wall Thickness for  $^{241}\text{Am}$  Source at 1 mm pressure and  $74^{\circ}\text{F}$

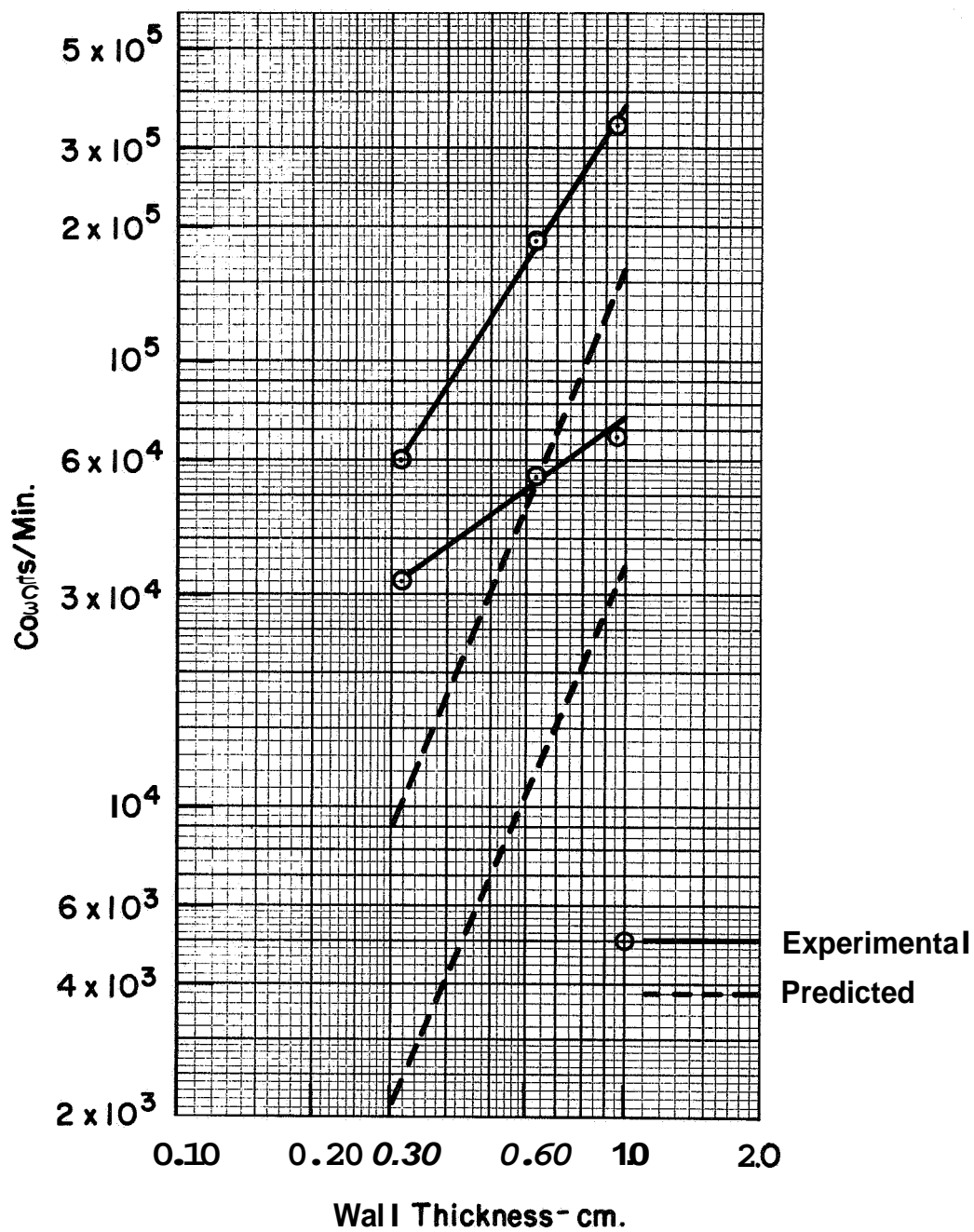


Fig. 10. Net Experimental Response and Predicted Response To Wall Thickness for  $^{153}\text{Gd}$  Source at 1 mm Pressure and  $64^{\circ}\text{F}$

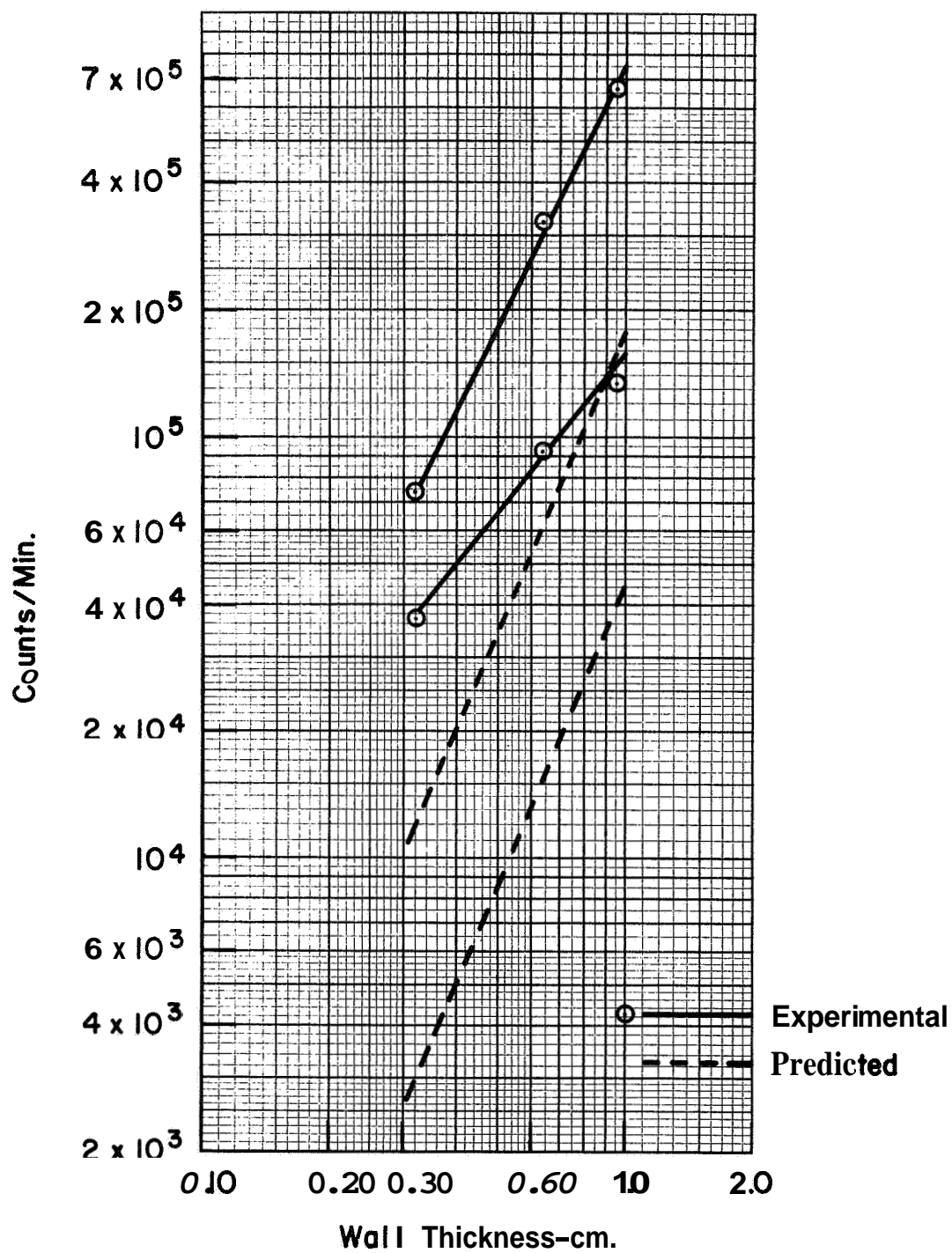


Fig. 11. Net Experimental Response and Predicted Response To Wall Thickness for  $^{57}\text{Co}$  Source at 1 mm Pressure and  $72^{\circ}\text{F}$

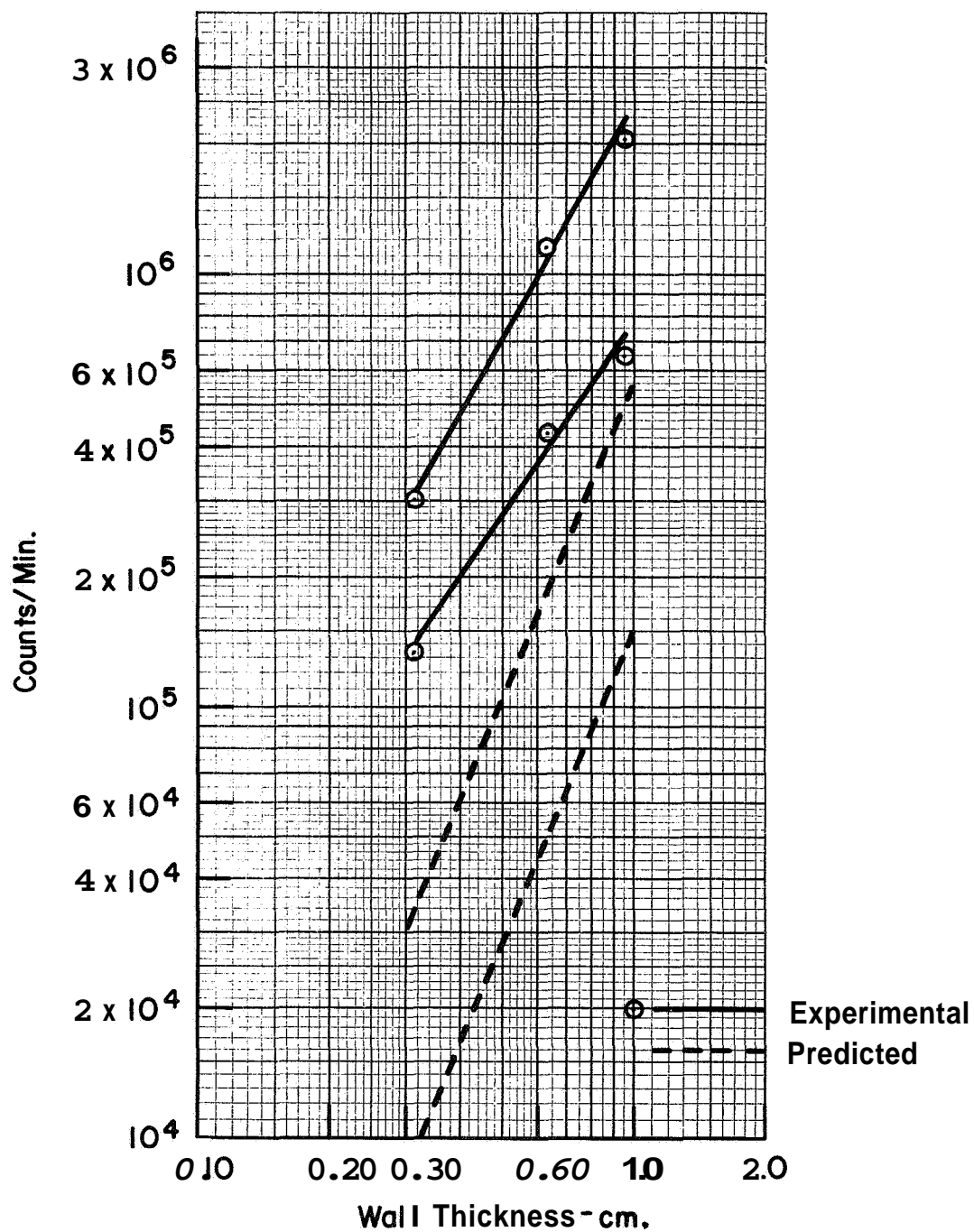
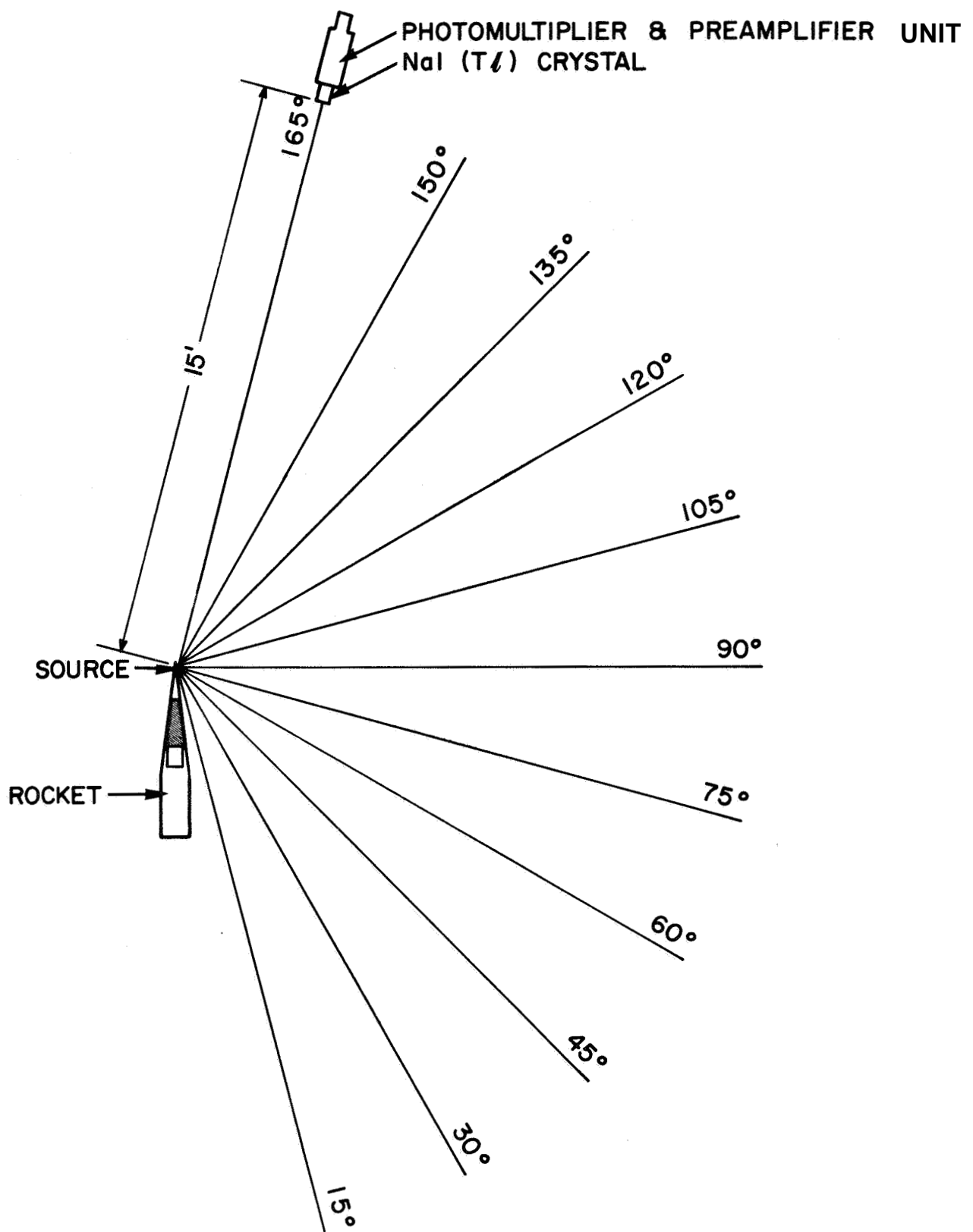


Fig. 12. Plan View of the bremsstrahlung Experimental Geometry



K&E SEMI-LOGARITHMIC 46 6213  
 5 CYCLES X 70 DIVISIONS  
 KEUFFEL & ESSER CO.

Net Counts/Min.

Fig. 13. Typical Spectra from the  $^{144}\text{Ce}$  Source at  $90^\circ$  from the Rocket Axis With the Tungsten Shield On and Off the Source

Calibration Data

- Shield open. Energy = 0.026057 (Channel No.) - 0.19017
  - × Shield closed. Energy = 0.025677 (Channel No.) - 0.15093
- (Energy Units are in Mev)

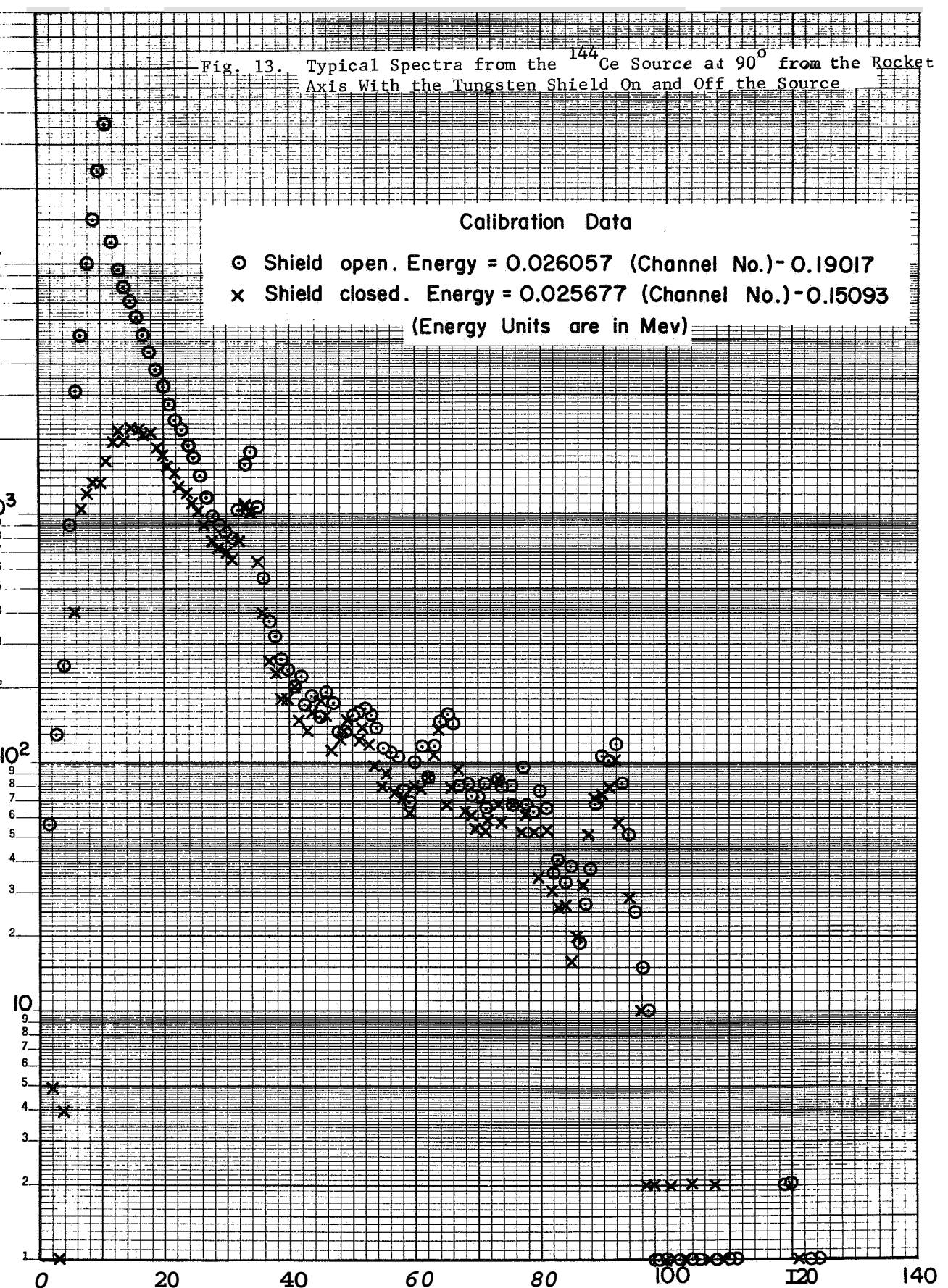


Fig. 14. Idealized Shape Assumed for Pulse-Height Spectra

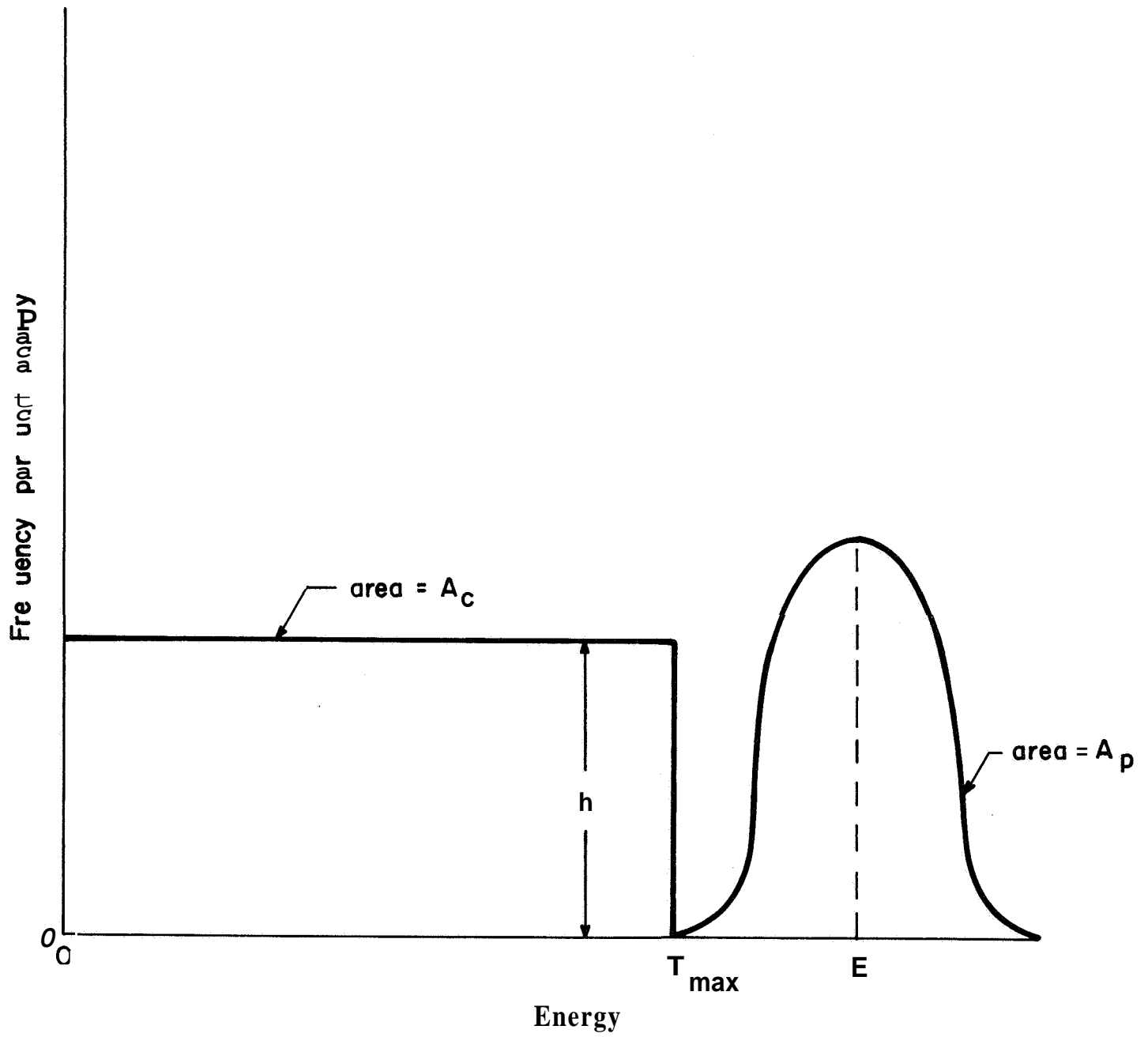


Fig. 15. Illustration of Splitting the Idealized Pulse-Height Spectra into Various Energy Intervals

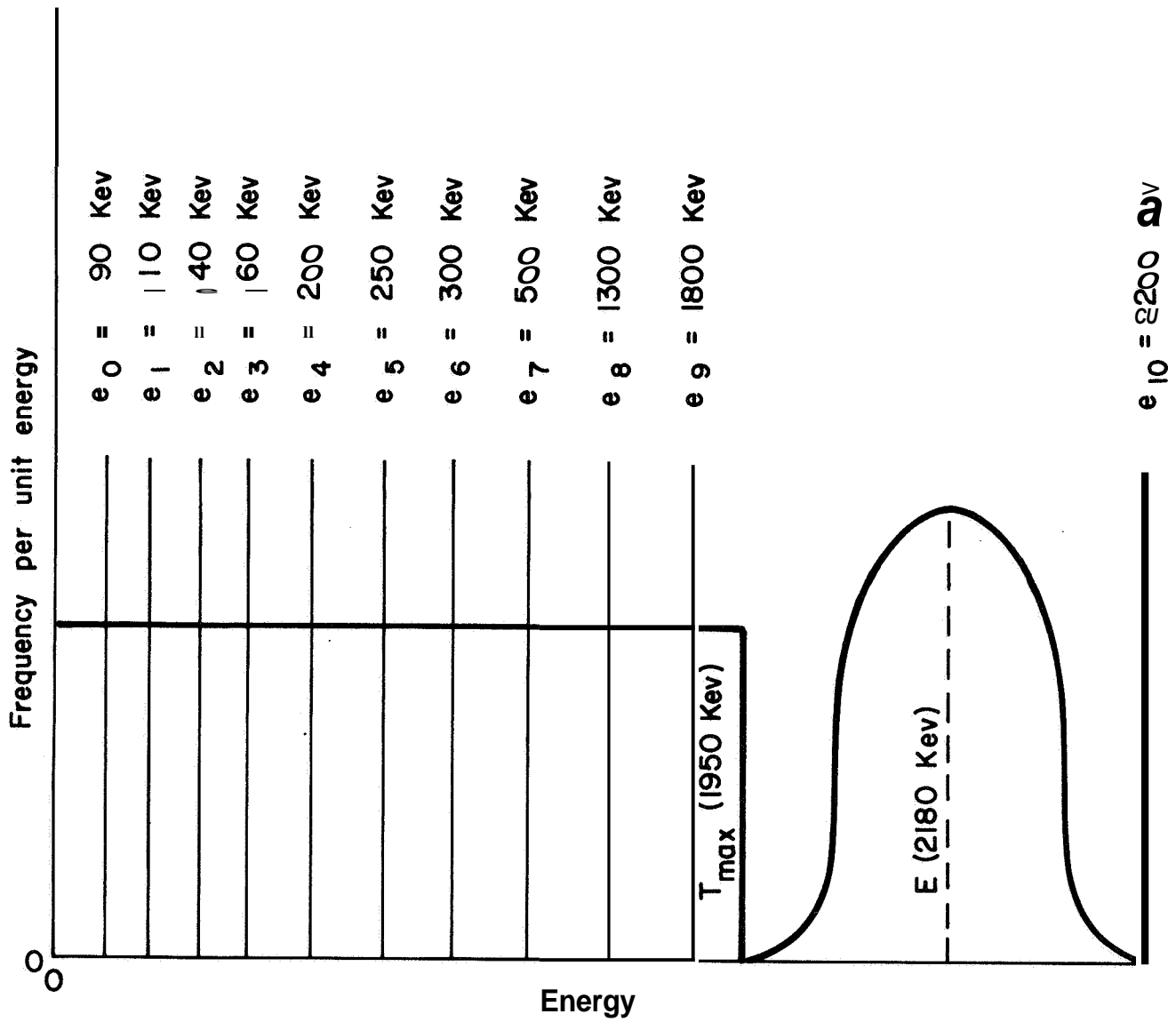


Table 1

Predicted Responses to Density and Wall Streaming for  
All Prototype Gauge Experimental Conditions

<u>Source</u>	<u>Average Source Energy</u> (Mev)	<u>Source-to- Detector Distance</u> (cm)	<u>Wall Thickness</u> (cm)	Predicted Fraction of Total Emitted Gamma Rays Detected Due to, <u>Wall Streaming</u> (For $2\pi$ Geometry)	Predicted Fraction of Total Emitted Gamma Rays Detected Due to <u>Unit Atmospheric Density</u> *
$^{241}\text{Am}$	0.060	14.21	0		$.2245 \times 10^{-4}$
			0.3175	$.1329 \times 10^{-6}$	
			0.6350	$.7195 \times 10^{-6}$	
			0.9525	$.1902 \times 10^{-5}$	
		10.40	0		$.3382 \times 10^{-4}$
			0.3175	$.6184 \times 10^{-6}$	
			0.6350	$.3379 \times 10^{-5}$	
			0.9525	$.9013 \times 10^{-5}$	
$^{153}\text{Gd}$	0.100	14.21	0		$.1880 \times 10^{-4}$
			0.3175	$.1876 \times 10^{-6}$	
			0.6350	$.1015 \times 10^{-5}$	
			0.9525	$.2674 \times 10^{-5}$	
		10.40	0		$.2840 \times 10^{-4}$
			0.3175	$.7301 \times 10^{-6}$	
			0.6350	$.3989 \times 10^{-5}$	
			0.9525	$.1058 \times 10^{-4}$	
$^{57}\text{Co}$	0.125	14.21	0		$.1642 \times 10^{-4}$
			0.3175	$.1918 \times 10^{-6}$	
			0.6350	$.1038 \times 10^{-5}$	
			0.9525	$.2732 \times 10^{-5}$	
		10.40	0		$.2486 \times 10^{-4}$
			0.3175	$.7082 \times 10^{-6}$	
			0.6350	$.3917 \times 10^{-5}$	
			0.9525	$.1040 \times 10^{-4}$	

\* These values should be multiplied by 1/6 to obtain the numbers appropriate for a  $60^\circ$  collimation.

Table 2

## Calibration Data for Radioisotope Sources

 $^{241}\text{Am}$ ,  $^{153}\text{Gd}$ , and  $^{57}\text{Co}$ 

<u>Source</u>	<u>Experimental Net Counting Rate at 27 Feet</u> (c/m)	<u>Effective Emission Rate*</u> (c/m)	<u>Experimental Effective Activity</u> (curies)	<u>Nominal Total Activity</u> (curies)
$^{241}\text{Am}$	$2.2513 \times 10^5$	$9.529 \times 10^{10}$	0.107	0.480
$^{153}\text{Gd}$	$2.1482 \times 10^5$	$9.093 \times 10^{10}$	0.089	0.050
$^{57}\text{Co}$	$6.7549 \times 10^5$	$2.859 \times 10^{11}$	0.131	0.150

---

\* These values were calculated from Eq. 1.3-1 with the experimental net counting rates at 27 feet.

Table 3

Experimental Responses to Density and Wall Streaming  
for All Prototype Gauge Experimental Conditions

<u>Source</u>	<u>Run No.</u>	<u>Source-to-Detector Distance</u>	<u>Wall Thickness</u>	<u>Pressure</u>	<u>Gross Counting Rate</u>
		(cm)	(cm)	(mm Hg)	(c/m)
$^{241}\text{Am}$	3	14.21	0	765	327,426
	7			691.5	299,536
	8			595	266,238
	9			496.5	223,980
	10			400.5	183,411
	11			300.5	139,885
	12			200	93,751
	13			100.75	48,167
	14			49.5	23,937
	15			19.5	10,788
	16			1.08	3,066
	17		0.3175	1.0	35,238
	18		0.6350	1.0	58,800
	19		0.9525	1.0	70,820
	20		0.9525	1.0	71,409
	24	10.40	0.9525	1.0	337,820
	25		0.6350	1.0	188,017
	26		0.3175	1.0	63,147
	27		0	1.0	3,371
	28		0	1.0	3,326
	29	10.40	0	52	26,909
	30			99.5	48,683
	31			195	90,200
	32			290.5	134,129
	33			391.5	179,027
	34			499.5	223,340
	35			596.5	264,954
	36			699	309,629
	37			763.6	346,383
$^{153}\text{Gd}$	45	14.21	0	763.6	283,984
	46			700.5	262,987
	47			599	232,577
	48			499.5	201,294
	49			398.5	166,744
	50			301	131,646
	51			201	94,448
	52			96.5	56,992
	53			1.05	20,514
	54		0.3175	1.0	57,601
	55		0.6350	1.0	111,934
	56		0.9525	1.0	157,293
	57		0.9525	1.0	156,837
	61		0.9525	1.0	709,140

Table 3 (Cont'd)

<u>Source</u>	<u>Run No.</u>	<u>Source-to-Detector Distance</u>	<u>Wall Thickness</u>	<u>Pressure</u>	<u>Gross Counting Rate</u>
<sup>153</sup> Gd	62	10.40	0.6350	1.0	349,133
	63		0.3175	1.0	103,523
	64		0	1.0	29,772
	65		0	1.0	29,932
	67			94	68,960
	68			199	102,794
	69			299	140,005
	70			400	175,216
	71			498	208,651
	72			598.5	258,141
	73			699.5	297,339
	74			763.2	312,583
<sup>57</sup> Co	78	14.21	0	763.2	787,231
	81			763.2	779,813
	82			690	725,722
	83			594	650,949
	84			500	569,400
	85			400.5	480,260
	86			297.5	385,065
	87			200	307,558
	88			1.08	103,365
	89			1.0	240,195
	90	14.21	0.6350	1.0	534,891
	91		0.9525	1.0	746,708
	92		0.9525	1.0	751,730
	94		0.9525	1.0	2,203,387
	96	10.40	0.9525	1.0	2,149,732
	97		0.6350	1.0	1,296,096
	98		0.3175	1.0	440,470
	99		0	1.0	142,616
	100		0	1.0	138,464
	104		0	97	240,475
	105		0	199.5	353,918
	106		0	301	444,276
	107		0	402	535,497
	108		0	499	628,947
	109		0	598.5	717,315
	110		0	698.5	800,435
	111		0	762	875,915

Table 4

Comparison of Experimental and Predicted Responses to Density  
and Wall Streaming for the Prototype Gauge

<u>Source</u>	<u>Source-to-Detector Distance</u> (cm)	<u>Wall Thickness</u> (cm)	<u>Air Pressure</u> * (mm Hg)	<u>Predicted Counting Rate</u> (c/m)	<u>Experimental Net Counting Rate</u> (c/m)	<u>Ratio of Experimental to Predicted</u>
$^{241}\text{Am}$	14.21	0	760	356,600	327,400**	0.918
		0.3175	0	2,110	32,170	15.25
		0.6350	0	11,430	55,730	4.88
		0.9525	0	30,200	68,040	2.25
	10.40	0	760	537,100	346,400**	0.645
		0.3175	0	9,822	59,800	6.09
		0.6350	0	53,670	184,700	3.44
		0.9525	0	143,100	334,500	2.34
	14.21	0	760	285,000	284,000**	0.996
		0.3175	0	2,843	37,090	13.05
		0.6350	0	15,380	91,390	5.94
		0.9525	0	40,520	136,600	3.37
$^{153}\text{Gd}$	10.40	0	760	430,400	312,600**	0.726
		0.3175	0	11,060	73,730	6.67
		0.6350	0	60,380	319,300	5.29
		0.9525	0	160,400	679,300	4.24
	14.21	0	760	782,500	783,500**	1.001
		0.3175	0	9,135	136,900	14.99
		0.6350	0	49,450	431,600	8.73
		0.9525	0	130,200	645,900	4.96
	10.40	0	760	1,185,000	876,000**	0.739
		0.3175	0	33,740	300,000	8.89
		0.6350	0	186,700	1,156,000	6.19
		0.9525	0	495,500	2,037,000	4.11
$^{57}\text{Co}$	14.21	0	760	782,500	783,500**	1.001
		0.3175	0	9,135	136,900	14.99
		0.6350	0	49,450	431,600	8.73
		0.9525	0	130,200	645,900	4.96
	10.40	0	760	1,185,000	876,000**	0.739
		0.3175	0	33,740	300,000	8.89
		0.6350	0	186,700	1,156,000	6.19
		0.9525	0	495,500	2,037,000	4.11

---

 \*

The zero values reported were actually about 1 mmHg.

\*\*

These values were taken from the best straight line drawn through all plotted experimental density results.

Table 5

Pulse-height Frequencies in Various Energy Intervals for  
Shield Open and **Closed Cases** at Fixed Angles

<u>Angle</u>	<u>90 Kev to 110 Kev</u>	<u>110 Kev to 140 Kev</u>	<u>140 Kev to 160 Kev</u>	<u>160 Kev to 200 Kev</u>
(degrees)	(c/m)	(c/m)	(c/m)	(c/m)
15o	516	630	462	746
15C	494	769	581	986
30o	1,144	1,814	1,104	2,340
30C	598	980	731	1,511
45o	1,722	2,411	1,581	3,013
45c	1,289	1,850	1,428	2,523
60o	1,785	2,480	1,739	3,592
60C	1,156	2,254	1,559	3,036
75o	2,543	3,936	2,334	4,866
75c	1,346	2,292	1,670	3,151
90o	15,178	12,879	6,181	12,204
90C	1,160	1,951	1,634	3,435
105o	11,646	15,042	5,458	8,970
105C	1,355	2,400	1,421	3,211
120o	1,870	2,858	2,256	4,527
120C	1,401	2,397	1,530	3,620
135o	1,567	2,473	1,895	3,657
135C	1,009	1,762	1,376	2,763
150o	1,735	2,198	1,337	2,659
150C	965	1,687	968	1,983
165o	932	1,429	936	1,634
165C	612	1,196	638	1,285

o Refers to source shield open or unshielded position.

C Refers to source shield closed or shielded position.

Table 5 (Cont'd)

<u>Angle</u>	<u>200 Kev</u> <u>to 250 Kev</u>	<u>250 Kev</u> <u>to 300 Kev</u>	<u>300 Kev</u> <u>to 500 Kev</u>	<u>500 Kev</u> <u>to 1300 Kev</u>	<u>1300 Kev</u> <u>to 1800 Kev</u>	<u>1800 Kev</u> <u>to 2300 Kev</u>
(degrees)	(c/m)	(c/m)	(c/m)	(c/m)	(c/m)	(c/m)
15 <sup>o</sup>	782	615	1,731	2,322	465	360
15C	1,061	852	2,097	2,616	524	341
30 <sup>o</sup>	2,551	1,551	4,440	4,819	851	515
30C	1,837	1,482	4,308	4,795	798	474
45 <sup>o</sup>	3,359	2,630	7,470	8,019	1,125	736
45c	3,059	2,560	7,320	7,857	1,110	698
60 <sup>o</sup>	3,914	3,470	9,423	9,481	1,395	817
60C	4,046	3,428	10,150	9,881	1,359	914
75 <sup>o</sup>	5,381	4,784	11,927	11,136	1,418	1,048
75c	3,817	3,836	10,301	10,323	1,345	861
90 <sup>o</sup>	10,986	8,096	17,164	14,095	1,814	1,160
90C	4,181	4,243	11,584	11,120	1,495	899
105 <sup>o</sup>	9,703	7,047	15,488	12,739	1,613	944
105c	3,809	3,450	9,889	9,759	1,325	883
120 <sup>o</sup>	5,425	4,727	11,907	11,278	1,538	1,009
120c	3,988	3,674	10,164	10,004	1,427	914
135 <sup>o</sup>	4,266	3,525	9,180	9,462	1,340	843
135C	3,244	2,781	8,134	8,510	1,277	765
150 <sup>o</sup>	2,600	2,039	4,743	5,750	1,005	596
150C	1,811	1,442	4,354	5,438	930	577
165 <sup>o</sup>	1,485	1,119	2,047	1,961	439	246
165C	1,113	662	1,701	1,947	393	244

<sup>o</sup> Refers to source shield open or unshielded position.

<sup>C</sup> Refers to source shield closed or shielded position.

Table 6

Model Predictions for Various Gamma-ray Energy Intervals  
and Angular Integration Limits

## Basic Model

## Gamma-Ray Energies

<u>Angle Ranges</u> (degrees)	<u>100 Kev</u>	<u>125 Kev</u>	<u>150 Kev</u>	<u>180 Kev</u>	<u>225 Kev</u>
10-40	$1.2325 \times 10^{-5}$	$3.7680 \times 10^{-5}$	$5.3133 \times 10^{-5}$	$4.1679 \times 10^{-5}$	$2.5501 \times 10^{-5}$
40-80	$6.4867 \times 10^{-7}$	$9.1151 \times 10^{-6}$	$1.9179 \times 10^{-5}$	$1.7712 \times 10^{-5}$	$1.3636 \times 10^{-5}$
80-100	$7.2485 \times 10^{-9}$	$3.1540 \times 10^{-6}$	$1.0760 \times 10^{-5}$	$1.0153 \times 10^{-5}$	$8.6496 \times 10^{-6}$
100-120	$1.9671 \times 10^{-10}$	$1.4147 \times 10^{-6}$	$7.4444 \times 10^{-6}$	$7.1079 \times 10^{-6}$	$6.0939 \times 10^{-6}$
120-140	$1.0876 \times 10^{-11}$	$5.4768 \times 10^{-7}$	$4.8081 \times 10^{-6}$	$4.6738 \times 10^{-6}$	$3.9992 \times 10^{-6}$
140-170	$3.7544 \times 10^{-13}$	$1.6668 \times 10^{-7}$	$2.2803 \times 10^{-6}$	$2.2754 \times 10^{-6}$	$1.9483 \times 10^{-6}$

## Gamma-Ray Energies

<u>Angle Ranges</u> (degrees)	<u>275 Kev</u>	<u>400 Kev</u>	<u>900 Kev</u>	<u>1550 Kev</u>	<u>2000 Kev</u>
10-40	$1.6789 \times 10^{-5}$	$3.0499 \times 10^{-6}$	$1.5542 \times 10^{-6}$	$9.9241 \times 10^{-7}$	$8.3770 \times 10^{-7}$
40-80	$9.4453 \times 10^{-6}$	$1.2713 \times 10^{-6}$	$4.4228 \times 10^{-7}$	$2.3767 \times 10^{-7}$	$2.1217 \times 10^{-7}$
80-100	$6.7037 \times 10^{-6}$	$9.7622 \times 10^{-7}$	$1.5088 \times 10^{-7}$	$9.3919 \times 10^{-8}$	$8.9030 \times 10^{-8}$
100-120	$5.0904 \times 10^{-6}$	$8.6143 \times 10^{-7}$	$7.4156 \times 10^{-8}$	$4.8334 \times 10^{-8}$	$4.8532 \times 10^{-8}$
120-140	$3.4329 \times 10^{-6}$	$7.2991 \times 10^{-7}$	$3.2326 \times 10^{-8}$	$2.3107 \times 10^{-8}$	$2.4415 \times 10^{-8}$
140-170	$1.6773 \times 10^{-6}$	$4.6263 \times 10^{-7}$	$1.5542 \times 10^{-8}$	$8.8215 \times 10^{-9}$	$9.7833 \times 10^{-9}$

Table 6 (Continued)

## Streaming Model

<u>Angle Ranges</u> (degrees)	<u>Gamma-Ray Energies</u>				
	<u>100 Kev</u>	<u>125 Kev</u>	<u>150 Kev</u>	<u>180 Kev</u>	<u>225 Kev</u>
10-40	$2.8808 \times 10^{-8}$	$9.5447 \times 10^{-8}$	$1.3412 \times 10^{-7}$	$1.0806 \times 10^{-7}$	$9.1424 \times 10^{-8}$
40-80	$1.0051 \times 10^{-9}$	$5.8003 \times 10^{-9}$	$9.7843 \times 10^{-9}$	$1.1135 \times 10^{-8}$	$9.0010 \times 10^{-9}$
80-100	$1.7541 \times 10^{-11}$	$1.1506 \times 10^{-9}$	$2.7527 \times 10^{-9}$	$3.9044 \times 10^{-9}$	$4.1532 \times 10^{-9}$
100-120	$3.7783 \times 10^{-13}$	$5.5084 \times 10^{-10}$	$1.5370 \times 10^{-9}$	$2.6592 \times 10^{-9}$	$3.4381 \times 10^{-9}$
120-140	$8.4950 \times 10^{-15}$	$1.9298 \times 10^{-10}$	$1.1074 \times 10^{-9}$	$2.2997 \times 10^{-9}$	$3.2296 \times 10^{-9}$
140-170	$2.9576 \times 10^{-16}$	$4.2348 \times 10^{-11}$	$1.0212 \times 10^{-9}$	$2.1869 \times 10^{-9}$	$3.7082 \times 10^{-9}$

<u>Angle Ranges</u> (degrees)	<u>Gamma-Ray Energies</u>				
	<u>275 Kev</u>	<u>400 Kev</u>	<u>900 Kev</u>	<u>1550 Kev</u>	<u>2000 Kev</u>
10-40	$4.2750 \times 10^{-8}$	$1.8596 \times 10^{-8}$	$2.5581 \times 10^{-8}$	$2.5562 \times 10^{-8}$	$2.4282 \times 10^{-8}$
40-80	$6.5769 \times 10^{-9}$	$3.1601 \times 10^{-9}$	$1.3728 \times 10^{-9}$	$1.4042 \times 10^{-9}$	$1.2965 \times 10^{-9}$
80-100	$3.2335 \times 10^{-9}$	$1.9988 \times 10^{-9}$	$6.1388 \times 10^{-10}$	$2.9012 \times 10^{-10}$	$2.3979 \times 10^{-10}$
100-120	$3.1593 \times 10^{-9}$	$2.3043 \times 10^{-9}$	$6.9437 \times 10^{-10}$	$4.2336 \times 10^{-10}$	$3.1182 \times 10^{-10}$
120-140	$3.5964 \times 10^{-9}$	$2.4876 \times 10^{-9}$	$9.6301 \times 10^{-10}$	$4.7354 \times 10^{-10}$	$3.8573 \times 10^{-10}$
140-170	$4.3701 \times 10^{-9}$	$3.8389 \times 10^{-9}$	$1.8477 \times 10^{-9}$	$8.5665 \times 10^{-10}$	$5.8475 \times 10^{-10}$

Table 7

Average Pulse-height Frequencies per Unit Solid Angle over Various  
Angular Intervals and Energy Intervals for Shield Open and Closed Cases

Experimental Spectra (cts/min)  
Shield Open

Energy Ranges

<u>Angles</u>	<u>100</u> <u>90-110</u>	<u>1</u> <u>110-140</u>	<u>15</u> <u>140-160</u>	<u>180</u> <u>160-200</u>	<u>225</u> <u>200-250</u>	<u>275</u> <u>250-300</u>	<u>400</u> <u>300-500</u>	<u>900</u> <u>500-1300</u>	<u>1550</u> <u>1300-1800</u>	<u>2000</u> <u>1800-∞</u>
10-40	920	1,430	920	1,790	1,920	1,235	3,520	3,970	720	440
40-80	2,020	2,880	1,860	3,800	4,190	3,635	9,650	9,500	1,330	840
80-100	12,600	10,925	5,120	10,000	9,650	7,265	15,830	13,275	1,800	1,120
100-120	8,350	11,040	4,370	7,450	8,250	6,250	14,260	12,300	1,600	960
120-140	1,650	2,600	2,000	3,950	4,670	3,880	10,100	10,100	1,400	860
140-170	1,510	1,920	1,180	2,340	2,200	1,770	4,170	4,540	810	460

Shield Closed

10-40	435	910	680	1,310	1,570	1,280	3,570	4,060	730	430
40-80	1,240	2,170	1,550	2,935	3,710	3,290	9,260	9,380	1,290	850
80-100	1,265	2,055	1,590	3,350	4,150	3,920	11,090	10,765	1,400	900
100-120	1,370	2,400	1,520	3,340	3,860	3,510	9,980	9,840	1,350	880
120-140	1,130	1,980	1,400	3,090	3,490	3,090	8,770	9,040	1,310	780
140-170	820	1,510	880	1,740	1,610	1,175	3,660	4,240	750	440

Table 8

Pulse-height Shape Factors and Total Detector Efficiencies Used to  
Convert Pulse-height Spectra to Gamma-ray Spectra

<u>Interval</u> <u>Energy</u>  (Kev)	<u><math>G(e_i, e_{i-1}, E_1)</math></u>	<u><math>G(e_i, e_{i-1}, E_2)</math></u>	<u><math>G(e_i, e_{i-1}, E_3)</math></u>	<u><math>E_T(E_i)</math></u>
2400-1800	0.276	---	---	0.432
1800-1300	0.278	0.289	---	0.482
1300- 500	0.444	0.615	0.449	0.617
500- 300	0.111	0.154	0.400	---
300- 250	0.028	0.038	0.100	---
250- 200	0.028	0.038	0.100	---
200- 160	0.022	0.031	0.080	---
160- 140	0.011	0.015	0.040	---
140- 110	0.017	0.023	0.060	---
110- 90	0.011	0.015	0.040	---

Table 9

Average Gamma-ray Frequencies per Unit Solid Angle over Various Angular  
Intervals and Energy Intervals for Shield Open and Closed Cases

Experimental Spectra (cts/min)  
Shield Open

Energy Ranges

Angles	100 90-110	125 110-140	150 140-160	180 160-200	225 200-250	275 250-300	400 300-500	900 500-1300	1550 1300-1800	2000 1800- $\infty$
10-40	752	1,178	752	1,454	1,500	815	1,841	10,298	2,872	3,686
40-80	1,604	2,255	1,444	2,968	3,149	2,594	5,486	26,831	5,161	7,036
80-100	12,016	10,048	4,536	8,831	8,189	5,804	9,986	37,833	7,071	9,381
100-120	7,806	10,224	3,826	6,362	6,890	4,890	8,820	35,440	6,468	8,042
120-140	1,207	1,934	1,557	3,064	3,561	2,771	5,666	28,614	5,556	7,204
140-170	1,318	1,631	988	1,956	1,718	1,288	2,244	11,858	3,410	3,853

Shield Closed

10-40	263	651	508	966	1,141	851	1,850	10,569	2,993	3,606
40-80	828	1,552	1,138	2,110	2,680	2,260	5,139	26,614	4,817	7,129
80-100	789	1,342	1,114	2,399	2,960	2,730	6,329	31,007	5,341	7,548
100-120	937	1,752	1,087	2,475	2,779	2,429	5,656	27,942	5,090	7,380
120-140	686	1,314	957	2,203	2,380	1,980	4,331	28,906	5,327	6,542
140-170	640	1,241	700	1,380	1,159	724	1,859	11,103	3,087	3,690

Table 10

Average Gamma-ray Frequencies per Unit Plane Angle over Various  
Angular Intervals and Energy Intervals for Shield Open and Closed Cases

<u>Angles</u>	Shield Open									
	<u>100</u> <u>90-110</u>	<u>125</u> <u>110-140</u>	<u>150</u> <u>140-160</u>	<u>180</u> <u>160-200</u>	<u>225</u> <u>200-250</u>	<u>275</u> <u>250-300</u>	<u>400</u> <u>300-500</u>	<u>900</u> <u>500-1300</u>	<u>1550</u> <u>1300-1800</u>	<u>2000</u> <u>1800-<math>\infty</math></u>
10-40	53	83	53	102	106	57	130	725	202	260
40-80	309	434	278	571	606	499	1056	5164	993	1354
80-100	1335	1116	504	981	910	645	1110	4204	786	1042
100-120	815	1067	399	664	719	511	921	3700	675	840
120-140	103	165	133	261	303	236	482	2435	473	613
140-170	93	115	70	138	121	91	158	835	240	271
Shield Closed										
10-40	19	46	36	68	80	60	130	744	211	254
40-80	159	299	219	406	516	435	989	5122	927	1372
80-100	88	149	124	267	329	303	703	3445	593	839
100-120	98	183	113	258	290	254	591	2917	531	771
120-140	58	112	81	187	203	169	369	2460	453	557
140-170	45	87	49	97	82	51	131	782	217	260

Table 11

Products of Model Predictions per Unit Source Emission and Total Number of  
Source Emissions for Various Angle Intervals and Gam-ray Energy  
Intervals for Shield Open and Closed and for Density  
and Wall Streaming Predictions

## Basic Model

<u>Angle Ranges</u> (degrees)	Shield Open				
	<u>100 Kev</u>	<u>125 Kev</u>	<u>150 Kev</u>	<u>180 Kev</u>	<u>225 Kev</u>
10-40	$6.5323 \times 10^{-4}$	$3.1274 \times 10^{-3}$	$2.8160 \times 10^{-3}$	$4.2513 \times 10^{-3}$	$2.7031 \times 10^{-3}$
40-80	$2.0044 \times 10^{-4}$	$3.9560 \times 10^{-3}$	$5.3318 \times 10^{-3}$	$1.0114 \times 10^{-2}$	$8.2634 \times 10^{-3}$
80-100	$9.6767 \times 10^{-6}$	$3.5199 \times 10^{-3}$	$5.4230 \times 10^{-3}$	$9.9601 \times 10^{-3}$	$7.8711 \times 10^{-3}$
100-120	$1.6032 \times 10^{-7}$	$1.5095 \times 10^{-3}$	$2.9703 \times 10^{-3}$	$4.7196 \times 10^{-3}$	$4.3815 \times 10^{-3}$
120-140	$1.1202 \times 10^{-9}$	$9.0367 \times 10^{-5}$	$6.3948 \times 10^{-4}$	$1.2199 \times 10^{-3}$	$1.2118 \times 10^{-3}$
140-170	$3.4916 \times 10^{-11}$	$2.7502 \times 10^{-5}$	$1.5962 \times 10^{-4}$	$3.1401 \times 10^{-4}$	$2.3574 \times 10^{-4}$
Shield Closed					
10-40	$2.3418 \times 10^{-4}$	$1.7333 \times 10^{-3}$	$1.9128 \times 10^{-3}$	$2.8342 \times 10^{-3}$	$2.0401 \times 10^{-3}$
40-80	$1.0314 \times 10^{-4}$	$2.7254 \times 10^{-3}$	$4.2002 \times 10^{-3}$	$7.1911 \times 10^{-3}$	$7.0362 \times 10^{-3}$
80-100	$6.3787 \times 10^{-7}$	$4.6995 \times 10^{-4}$	$1.3342 \times 10^{-3}$	$2.7108 \times 10^{-3}$	$2.8457 \times 10^{-3}$
100-120	$1.9278 \times 10^{-8}$	$2.5889 \times 10^{-4}$	$8.4122 \times 10^{-4}$	$1.8338 \times 10^{-3}$	$1.7672 \times 10^{-3}$
120-140	$6.3081 \times 10^{-10}$	$6.1340 \times 10^{-5}$	$3.8946 \times 10^{-4}$	$8.7400 \times 10^{-4}$	$8.1184 \times 10^{-4}$
140-170	$1.6895 \times 10^{-11}$	$1.4501 \times 10^{-5}$	$1.1173 \times 10^{-4}$	$2.2071 \times 10^{-4}$	$1.5976 \times 10^{-4}$

Table 11 (Continued)

## Basic Model

<u>Angle Ranges</u> (degrees)	Shield Open				
	<u>275 Kev</u>	<u>400 Kev</u>	<u>900 Kev</u>	<u>1550 Kev</u>	<u>2000 Kev</u>
10-40	$9.5697 \times 10^{-4}$	$3.9649 \times 10^{-4}$	$1.1268 \times 10^{-3}$	$2.0047 \times 10^{-4}$	$2.1780 \times 10^{-4}$
40-80	$4.7132 \times 10^{-3}$	$1.3425 \times 10^{-3}$	$2.2839 \times 10^{-3}$	$2.3601 \times 10^{-4}$	$2.8728 \times 10^{-4}$
80-100	$4.3239 \times 10^{-3}$	$1.0836 \times 10^{-3}$	$6.3430 \times 10^{-4}$	$7.3820 \times 10^{-5}$	$9.2769 \times 10^{-5}$
100-120	$2.6012 \times 10^{-3}$	$7.9338 \times 10^{-4}$	$2.7438 \times 10^{-4}$	$3.2625 \times 10^{-5}$	$4.0767 \times 10^{-5}$
120-140	$8.1016 \times 10^{-4}$	$3.5182 \times 10^{-4}$	$7.8714 \times 10^{-5}$	$1.0930 \times 10^{-5}$	$1.4966 \times 10^{-5}$
140-170	$1.5263 \times 10^{-4}$	$7.3096 \times 10^{-5}$	$1.2978 \times 10^{-5}$	$2.1172 \times 10^{-6}$	$2.6513 \times 10^{-6}$
Shield Closed					
10-40	$1.0073 \times 10^{-3}$	$3.9649 \times 10^{-4}$	$1.1563 \times 10^{-3}$	$2.0940 \times 10^{-4}$	$2.1278 \times 10^{-4}$
40-80	$4.1087 \times 10^{-3}$	$1.2573 \times 10^{-3}$	$2.2654 \times 10^{-3}$	$2.2032 \times 10^{-4}$	$2.9110 \times 10^{-4}$
80-100	$2.0312 \times 10^{-3}$	$6.8628 \times 10^{-4}$	$5.1978 \times 10^{-4}$	$5.5694 \times 10^{-5}$	$7.4696 \times 10^{-5}$
100-120	$1.2930 \times 10^{-3}$	$5.0911 \times 10^{-4}$	$2.1631 \times 10^{-4}$	$2.5665 \times 10^{-5}$	$3.7418 \times 10^{-5}$
120-140	$5.8016 \times 10^{-4}$	$2.6934 \times 10^{-4}$	$7.9522 \times 10^{-5}$	$1.0467 \times 10^{-5}$	$1.3599 \times 10^{-5}$
140-170	$8.5542 \times 10^{-5}$	$6.0605 \times 10^{-5}$	$1.2154 \times 10^{-5}$	$1.9143 \times 10^{-6}$	$2.5437 \times 10^{-6}$

Table 11 (Continued)

## Streaming Model

<u>Angle Ranges</u> (degrees)	Shield Open				
	<u>100 Kev</u>	<u>125 Kev</u>	<u>150 Kev</u>	<u>180 Kev</u>	<u>225 Kev</u>
10-40	$1.5268 \times 10^{-6}$	$7.0921 \times 10^{-6}$	$7.1084 \times 10^{-6}$	$1.1022 \times 10^{-5}$	$9.6909 \times 10^{-6}$
40-80	$3.1058 \times 10^{-7}$	$2.5173 \times 10^{-6}$	$2.7200 \times 10^{-6}$	$6.3581 \times 10^{-6}$	$5.4546 \times 10^{-6}$
80-100	$2.3297 \times 10^{-8}$	$1.2841 \times 10^{-6}$	$1.3874 \times 10^{-6}$	$3.8302 \times 10^{-6}$	$3.7794 \times 10^{-6}$
100-120	$3.0793 \times 10^{-10}$	$5.8775 \times 10^{-7}$	$6.1326 \times 10^{-7}$	$1.7657 \times 10^{-6}$	$2.4720 \times 10^{-6}$
120-140	$8.7499 \times 10^{-13}$	$3.1842 \times 10^{-8}$	$1.4728 \times 10^{-7}$	$6.0022 \times 10^{-7}$	$9.7857 \times 10^{-7}$
140-170	$2.7506 \times 10^{-14}$	$4.8700 \times 10^{-9}$	$7.1484 \times 10^{-8}$	$3.0179 \times 10^{-7}$	$4.4869 \times 10^{-7}$
Shield Closed					
10-40	$5.4735 \times 10^{-7}$	$3.9306 \times 10^{-6}$	$4.8283 \times 10^{-6}$	$7.3481 \times 10^{-6}$	$7.3139 \times 10^{-6}$
40-80	$1.5981 \times 10^{-7}$	$1.7343 \times 10^{-6}$	$2.1428 \times 10^{-6}$	$4.5208 \times 10^{-6}$	$4.6445 \times 10^{-6}$
80-100	$1.5357 \times 10^{-9}$	$1.7144 \times 10^{-7}$	$3.4133 \times 10^{-7}$	$1.0425 \times 10^{-6}$	$1.3664 \times 10^{-6}$
100-120	$3.7027 \times 10^{-11}$	$1.0080 \times 10^{-7}$	$1.7368 \times 10^{-7}$	$6.8607 \times 10^{-7}$	$9.9705 \times 10^{-7}$
120-140	$4.9271 \times 10^{-13}$	$2.1614 \times 10^{-8}$	$8.9699 \times 10^{-8}$	$4.3004 \times 10^{-7}$	$6.5561 \times 10^{-7}$
140-170	$1.3309 \times 10^{-14}$	$3.6843 \times 10^{-9}$	$5.0039 \times 10^{-8}$	$2.1213 \times 10^{-7}$	$3.0407 \times 10^{-7}$

Table 11 (Continued)

## Streaming Model

<u>Angle Ranges</u> (degrees)	Shield Open				
	<u>275 Kev</u>	<u>400 Kev</u>	<u>900 Kev</u>	<u>1550 Kev</u>	<u>2000 Kev</u>
10-40	$2.4368 \times 10^{-6}$	$2.4175 \times 10^{-6}$	$1.8546 \times 10^{-5}$	$5.1635 \times 10^{-6}$	$6.3133 \times 10^{-6}$
40-80	$3.2819 \times 10^{-6}$	$3.3371 \times 10^{-6}$	$7.0891 \times 10^{-6}$	$1.3944 \times 10^{-6}$	$1.7555 \times 10^{-6}$
80-100	$2.0856 \times 10^{-6}$	$2.2187 \times 10^{-6}$	$2.5808 \times 10^{-6}$	$2.2803 \times 10^{-7}$	$2.4986 \times 10^{-7}$
100-120	$1.6144 \times 10^{-6}$	$2.1223 \times 10^{-6}$	$2.5692 \times 10^{-6}$	$2.8577 \times 10^{-7}$	$2.6193 \times 10^{-7}$
120-140	$8.4875 \times 10^{-7}$	$1.1990 \times 10^{-6}$	$2.3449 \times 10^{-6}$	$2.2398 \times 10^{-7}$	$2.3645 \times 10^{-7}$
140-170	$3.9768 \times 10^{-7}$	$6.0655 \times 10^{-7}$	$1.5428 \times 10^{-6}$	$2.0560 \times 10^{-7}$	$1.5847 \times 10^{-7}$
Shield Closed					
10-40	$2.5650 \times 10^{-6}$	$2.4175 \times 10^{-6}$	$1.9032 \times 10^{-5}$	$5.3936 \times 10^{-6}$	$6.1676 \times 10^{-6}$
40-80	$2.8610 \times 10^{-6}$	$3.1253 \times 10^{-6}$	$7.0315 \times 10^{-6}$	$1.3017 \times 10^{-6}$	$1.7788 \times 10^{-6}$
80-100	$9.7975 \times 10^{-7}$	$1.4052 \times 10^{-6}$	$2.1148 \times 10^{-6}$	$1.7204 \times 10^{-7}$	$2.0118 \times 10^{-7}$
100-120	$8.0246 \times 10^{-7}$	$1.3618 \times 10^{-6}$	$2.0255 \times 10^{-6}$	$2.2480 \times 10^{-7}$	$2.4041 \times 10^{-7}$
120-140	$6.0779 \times 10^{-7}$	$9.1792 \times 10^{-7}$	$2.3690 \times 10^{-6}$	$2.1450 \times 10^{-7}$	$2.1485 \times 10^{-7}$
140-170	$2.2288 \times 10^{-7}$	$5.0290 \times 10^{-7}$	$1.4449 \times 10^{-6}$	$1.8589 \times 10^{-7}$	$1.5204 \times 10^{-7}$

Table 11 (Continued)

Totals		
<u>Angle Range</u>	<u>Basic Model Shield Open</u>	<u>Streaming Model Shield Open</u>
10-40	$1.6450 \times 10^{-2}$	$7.13173 \times 10^{-5}$
40-80	$3.6729 \times 10^{-2}$	$3.42186 \times 10^{-5}$
80-100	$3.2992 \times 10^{-2}$	$1.76674 \times 10^{-5}$
100-120	$1.7323 \times 10^{-2}$	$1.22926 \times 10^{-5}$
120-140	$4.4281 \times 10^{-3}$	$6.61099 \times 10^{-6}$
140-170	<u><math>9.8034 \times 10^{-4}</math></u>	<u><math>3.73793 \times 10^{-6}</math></u>
Total	$1.0890 \times 10^{-1} \approx 0.10890$	Total $1.45845 \times 10^{-4}$

<u>Angle Range</u>	<u>Basic Model Shield Closed</u>	<u>Streaming Model Shield Closed</u>
10-40	$1.1737 \times 10^{-2}$	$5.95440 \times 10^{-5}$
40-80	$2.9399 \times 10^{-2}$	$2.93005 \times 10^{-5}$
80-100	$1.0729 \times 10^{-2}$	$7.79618 \times 10^{-6}$
100-120	$6.7826 \times 10^{-3}$	$6.61261 \times 10^{-6}$
120-140	$3.0897 \times 10^{-3}$	$5.52105 \times 10^{-6}$
140-170	<u><math>6.6946 \times 10^{-4}</math></u>	<u><math>3.07853 \times 10^{-6}</math></u>
Total	$6.2407 \times 10^{-2} \approx 0.062407$	Total $1.11853 \times 10^{-4}$

$$\text{Ratio } \frac{\text{Open}}{\text{Closed}} = \frac{0.10890}{0.062407} \approx 1.745 \quad \text{Ratio } \frac{\text{Open}}{\text{Closed}} = \frac{1.45845}{1.11853} \approx 1.3039$$

Table 12

Source of Responses to Density and Wall Streaming  
with Shield Open and Closed

	<u>0.134-Mev Gamma Rays</u>	<u>Bremsstrahlung</u>	<u>High-Energy Gamma Rays</u>
Percentage of Total Emitted from Source			
Shield Open	16.4	26.3	57.3
Shield Closed	6.2	22.2	71.6
Percentage of Total Density Response			
Shield Open	27.9	66.9	5.2
Shield Closed	23.0	68.2	8.6
Percentage of Total Wall Streaming Response (Background)			
Shield Open	17.4	47.5	35.1
Shield Closed	13.1	40.9	46.0